Supplement of Atmos. Chem. Phys., 26, 7803–7826, 2026
https://doi.org/10.5194/acp-26-7803-2026-supplement

Atmospheric Chemistry and Physics
Open Access
EGU

Supplement of

Geostationary observations of atmospheric ammonia over East Asia: spatio-temporal variations revealed by three years of FY-4B/GIIRS measurements

Mengya Sheng et al.

Correspondence to: Zhao-Cheng Zeng (zczeng@pku.edu.cn)

S1. Calculation of the modelled NH_3 columns by applying satellite AVKs to GEOS-CF NH_3 profiles

In this study, GEOS-CF model data were used as a consistent and comparable reference to account for the vertical sensitivity of the satellite retrievals. The satellite retrievals operate on different vertical layers (GIIRS: ~12 layers; IASI: ~14 layers; CrIS: ~14 layers). The GEOS-CF NH_3 profiles collocated with the satellite observations were interpolated onto the instrument-specific retrieval layers. The GEOS-CF NH_3 profiles were initially interpolated onto each instrument's retrieval grid. Subsequently, the profiles were converted to total columns by using the satellite averaging kernels (AVKs) and a priori profiles according to the following equation:

$$\widehat{M}_{AVK,sat} = \sum_{z} A_z^{sat} \left(M_z^{model} - B_z \right) + B$$

where M_z^{model} represents GEOS-CF NH_3 profiles that have been interpolated onto the satellite-retrieved layer (z), A_z^{sat} is the satellite AVKs, B_z is the a priori profile used in the retrieval algorithm, and B corresponds to the total column associated with B_z. The resulting modelled NH_3 columns $\widehat{M}_{AVK,sat}$ are hereafter referred to as GEOS-$CF_{AVK,\ GIIRS}$, GEOS-$CF_{AVK,\ IASI}$, and GEOS-$CF_{AVK,\ CrIS}$ for GIIRS, IASI, and CrIS, respectively. As shown in Fig. S1(b), the a priori profile used in the IASI retrievals follows the method described in Clarisse et al. (2023), which provides only the vertical profile shape. In the calculation for IASI, B_z is assumed to be zero.

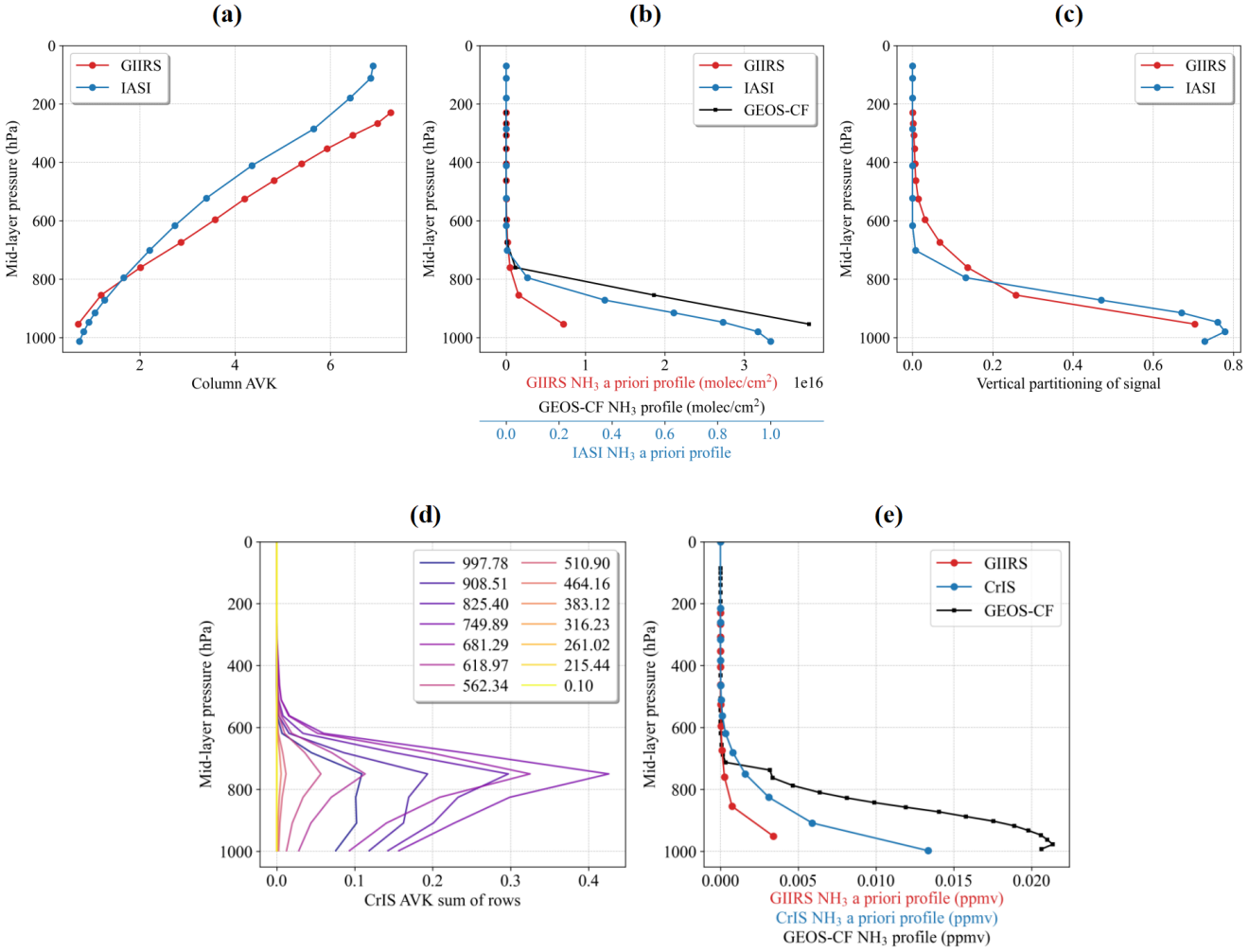

Figure S1. Illustration of satellite's AVKs and a priori profiles using two example retrievals over the North China Plain. Top panels show GIIRS and IASI observations near 38.35°N, 116.82°E on 9 June 2024. (a) Column AVKs from GIIRS and IASI. (b) The corresponding a priori profile from GIIRS and IASI, compared with GEOS-CF NH_3 profile, which have been interpolated onto GIIRS' retrieved layers. (c) Vertical partitioning signals of GIIRS and IASI, obtained by multiplying the column AVK with the normalized a priori profile. Bottom panels show GIIRS and CrIS observations near 38.04°N, 117.67°E on 14 June 2024. (d) Row sums of matrix AVK from CrIS. (e) Similar to (b), but for GIIRS, CrIS, and GEOS-CF without interpolating. For GIIRS, retrievals are performed below 200 hPa, and a single a priori profile is applied to all observations, in which the lowest layer is adjusted by interpolating to the surface pressure obtained from ERA5.

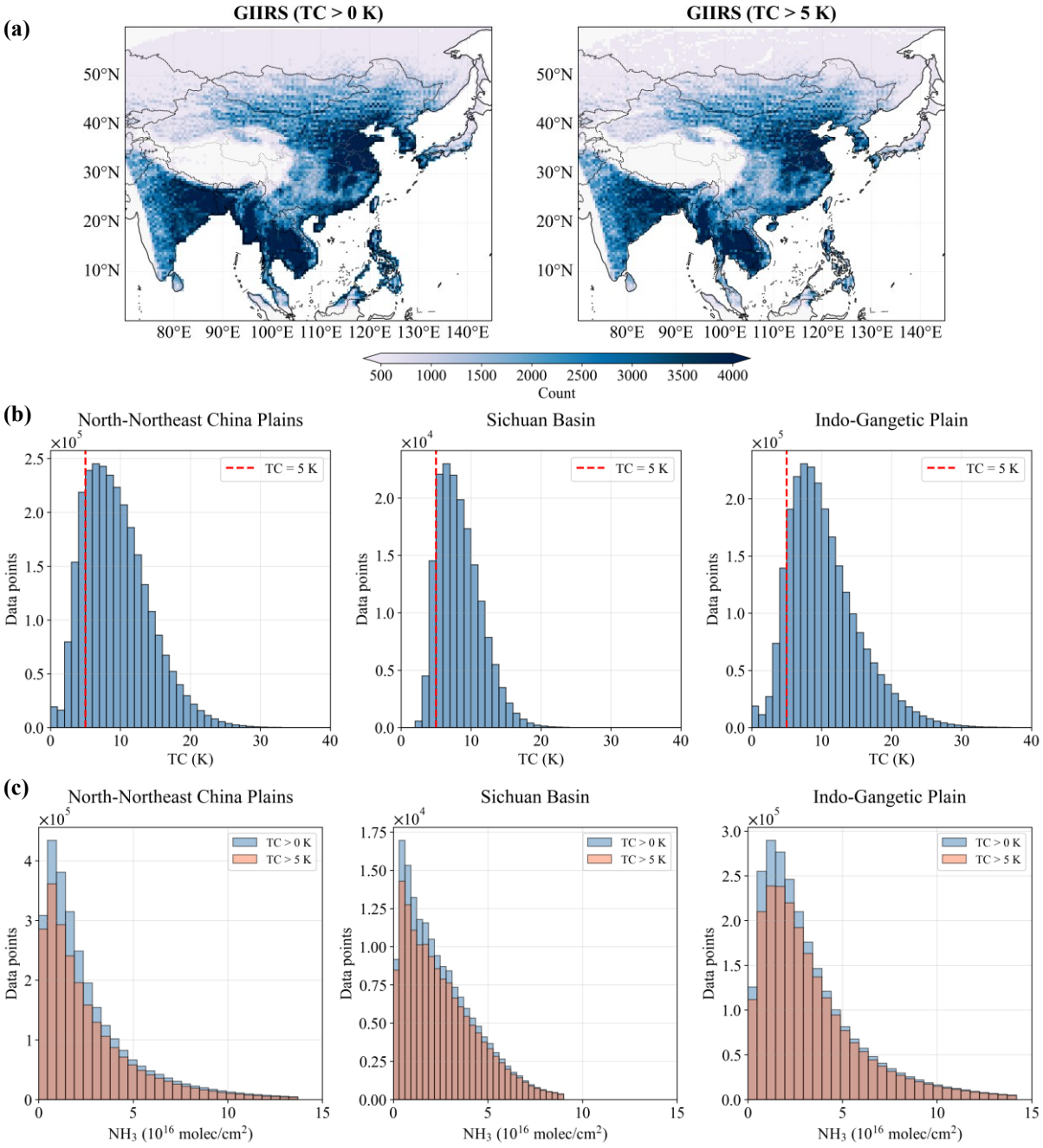

Figure S2. Valid data points of FY-4B/GIIRS NH_3 retrievals from July 2022 to June 2025. (a) Spatial distribution of data numbers under different TC thresholds at a 0.5° × 0.5° grid resolution. (b) Histogram of data points with TC > 0 K for three major emission regions shown in Fig. 1. (c) Histogram of NH_3 column concentrations using different TC thresholds for three major emission regions.

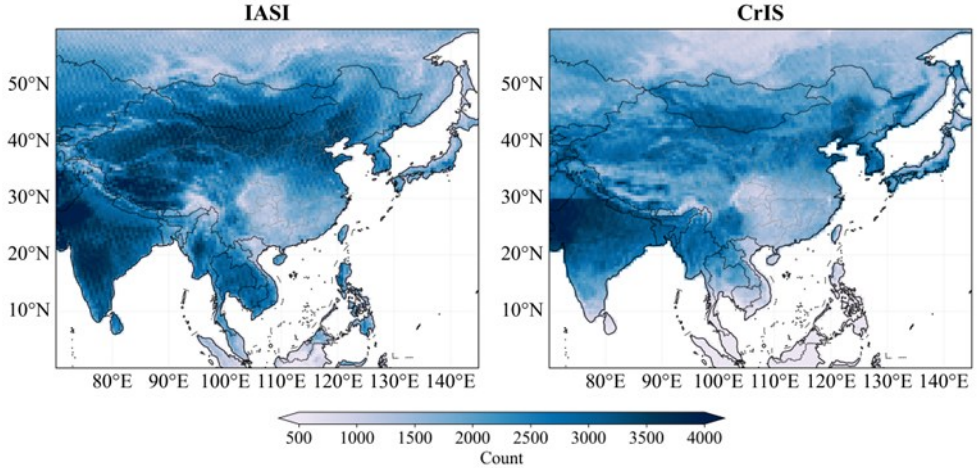

Figure S3. Valid data points of satellite NH_3 retrievals for IASI from July 2022 to June 2025 and for CrIS from July 2022 to April 2025 at a spatial scale of 0.5°×0.5° grid.

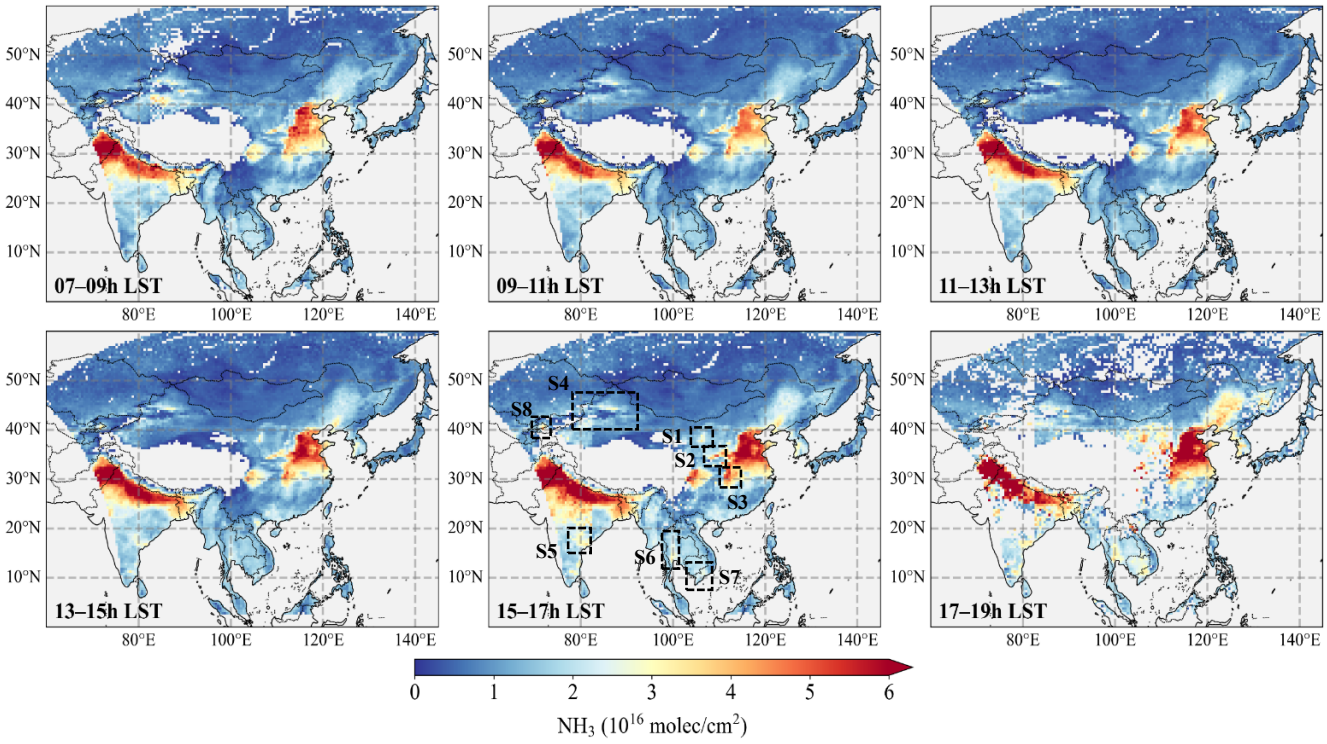

Figure S4. Three-year mean NH_3 columns retrieved from FY-4B/GIIRS observations between July 2022 and June 2025. The maps are displayed on a 0.5° × 0.5° grid at two-hour intervals, starting at local solar times of 07:00, 09:00, 11:00, 13:00, 15:00, and 17:00. Grid cells with less than 10 data points were excluded. The dashed boxes denote regions exhibiting localized enhancements of NH_3 columns: the Ningxia Irrigation Plain (S1), the Wei River Plain (S2), the Jianghan Plain (S3), and oasis agriculture in the arid regions of Xinjiang (S4), the central Deccan Plateau in India (S5), the Mekong Delta in Vietnam (S6), the Chao Phraya River Plain in Thailand (S7), and the Fergana Valley in Uzbekistan (S8).

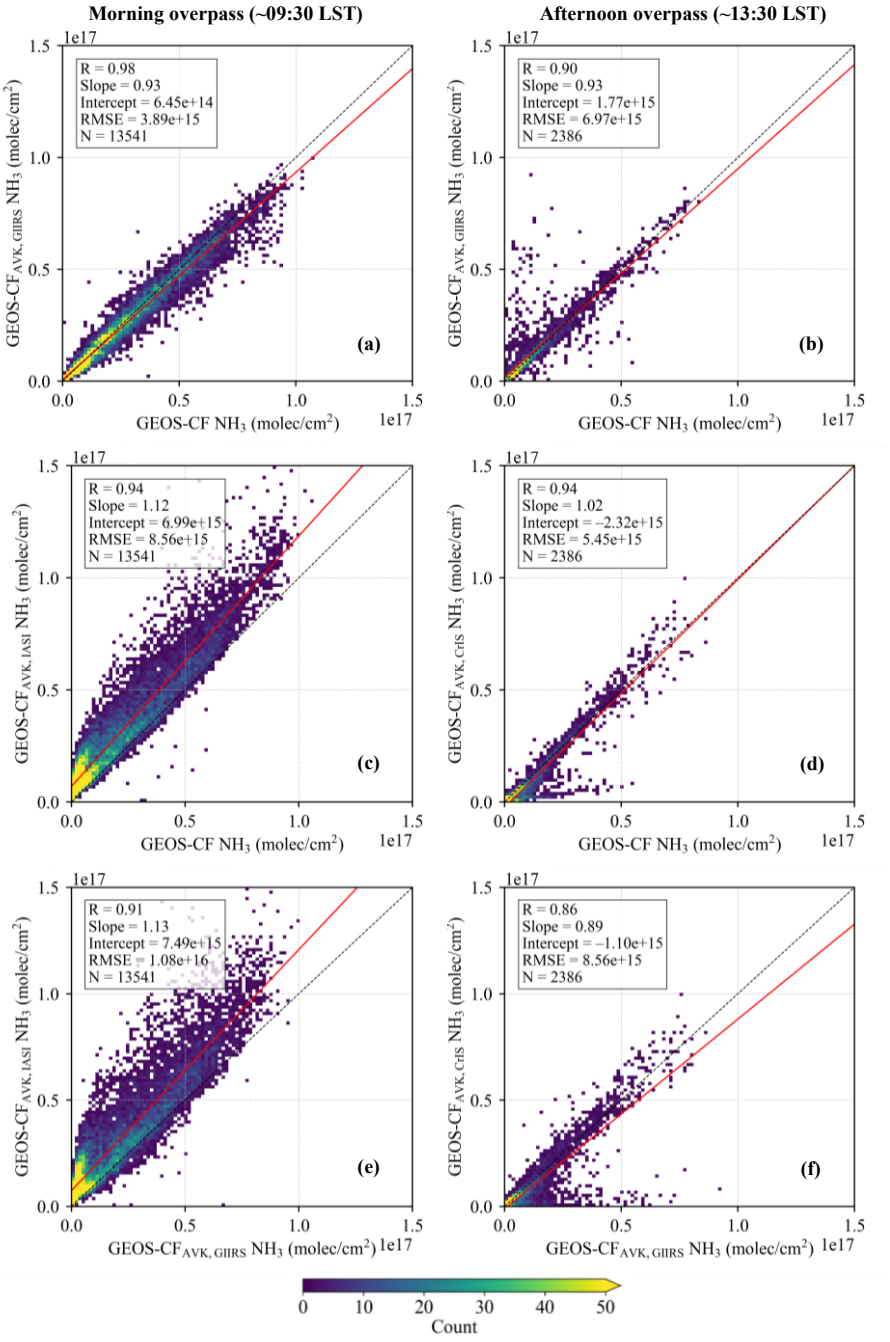

Figure S5. Comparison of the modelled NH_3 columns over the North-Northeast China Plains (30°–43°N, 110°–125°E) in June 2024, derived from GEOS-CF model profiles with satellite AVKs smoothing. Data pairs correspond to the same grid cells and overpass times. Panels (a) and (c) are comparisons of modelled NH_3 columns at morning overpass times after AVK smoothing for GIIRS and IASI, respectively, relative to the original total column values. Panels (b) and (d) are similar comparisons at afternoon overpass times for GIIRS and CrIS, respectively. Panels (e) and (f) show cross-comparisons between modelled NH_3 columns smoothed using different satellite AVKs: (e) GIIRS vs. IASI, and (f) GIIRS vs. CrIS.

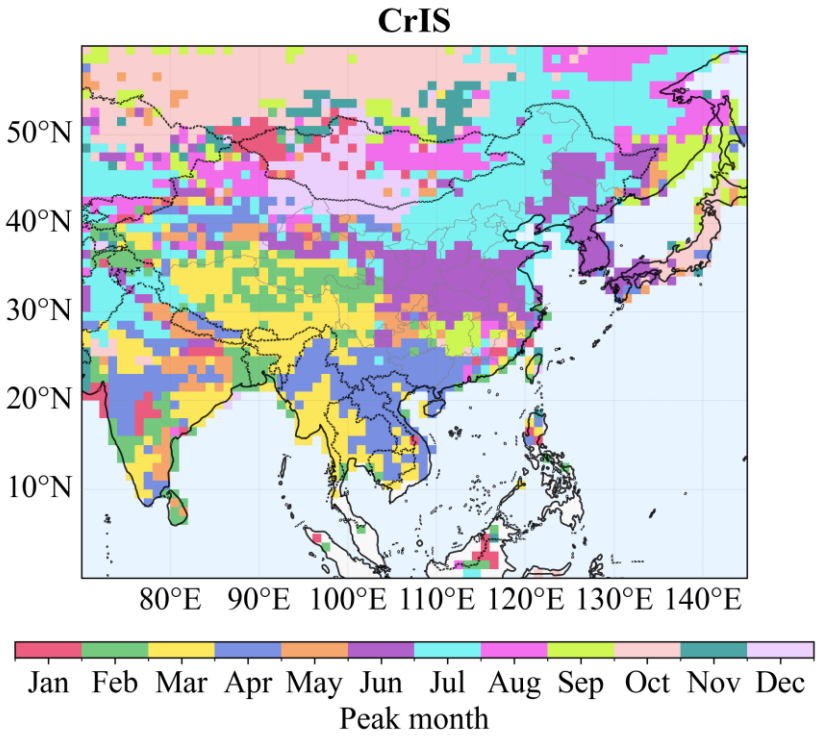

Figure S6. Same as Figure 5, but for CrIS retrievals from July 2022 to April 2025 at 1° grid.

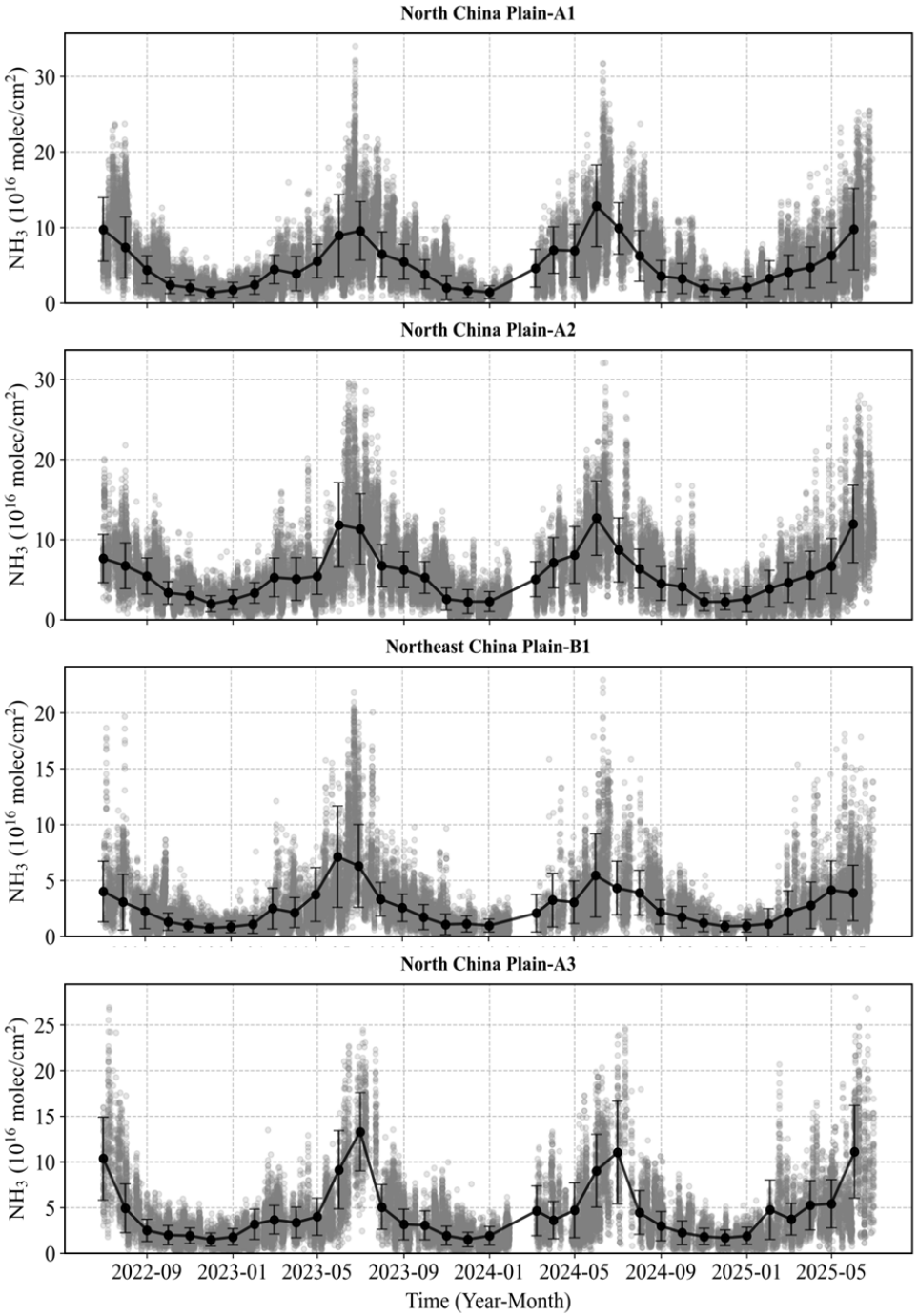

Figure S7. Monthly variations of NH_3 columns derived from GIIRS (July 2022–June 2025) for eight agricultural source areas.

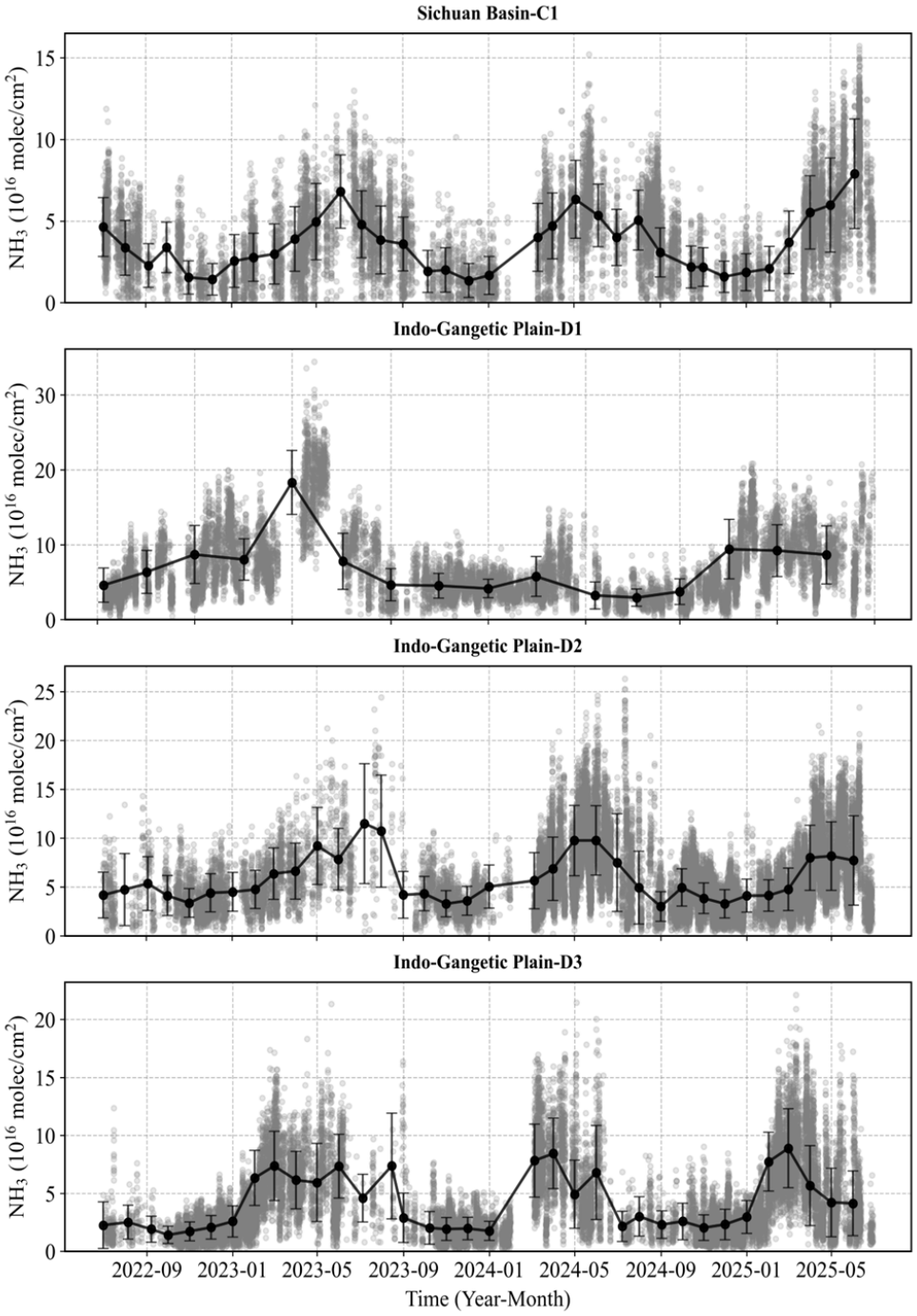

Figure S7 (continued). Monthly variations of NH_3 columns derived from GIIRS (July 2022–June 2025) for eight agricultural source areas.

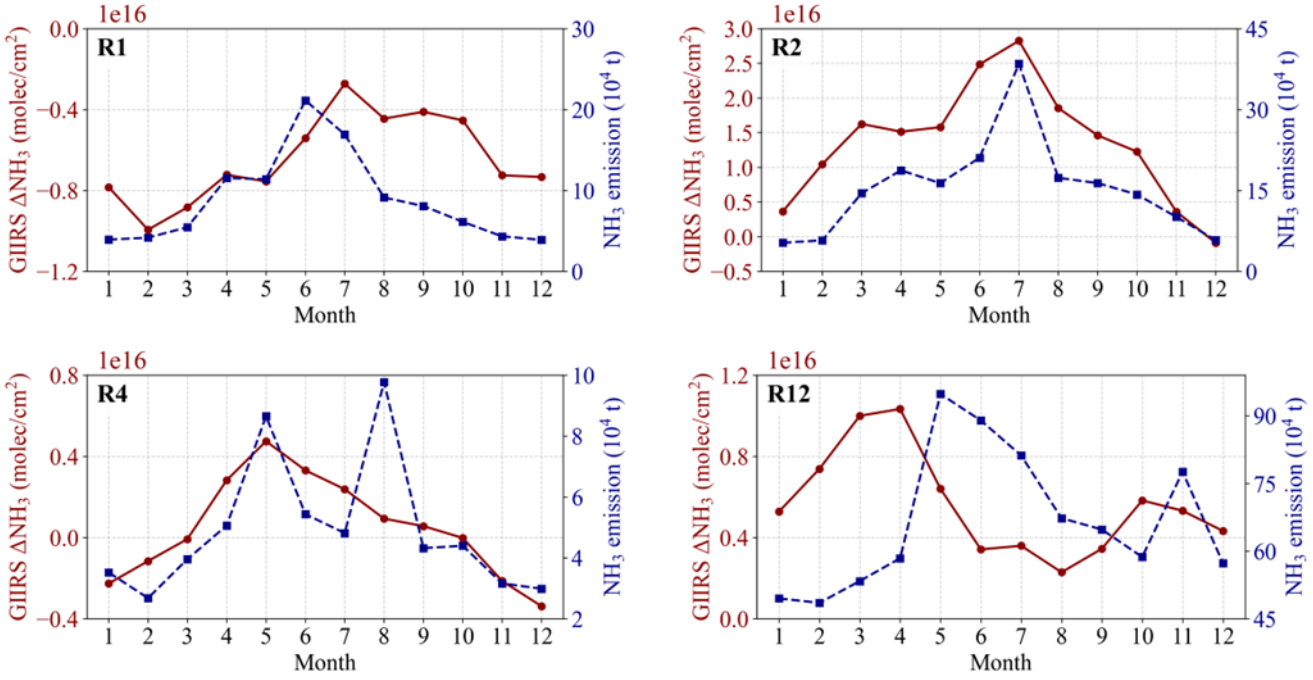

Figure S8. Comparison of seasonal cycles of GIIRS-observed NH_3 columns and MIX-based NH_3 emissions. ΔNH_3 are regional NH_3 variations relative to the background level over East Asia, primarily reflecting concentration changes associated with local anthropogenic emissions and meteorological conditions. The four regions correspond to the subregions defined in Fig. 6.

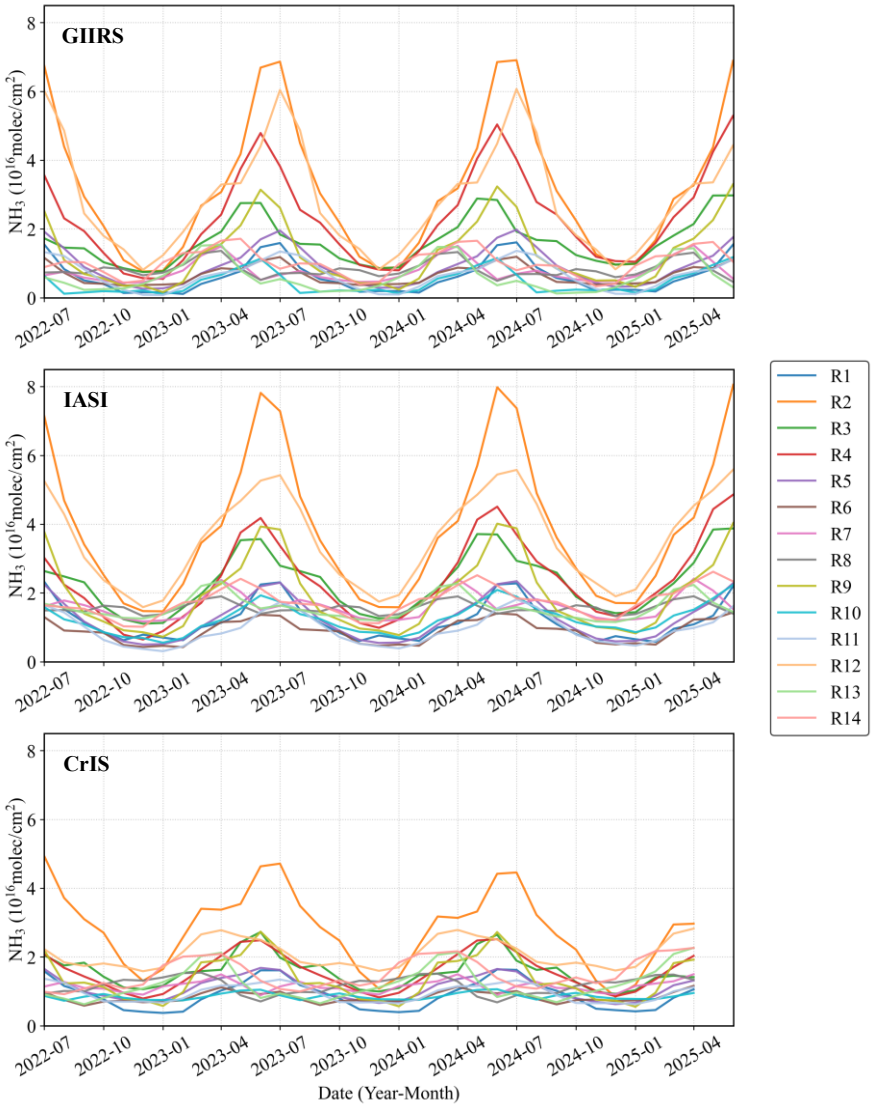

Figure S9. Monthly backgrounds of NH_3 columns derived from predefined regions using GIIRS (daytime overpass times, 7:00–19:00 LST), IASI (morning overpass times, ~9:30 LST), and CrIS observations (afternoon overpass times, ~13:30 LST).

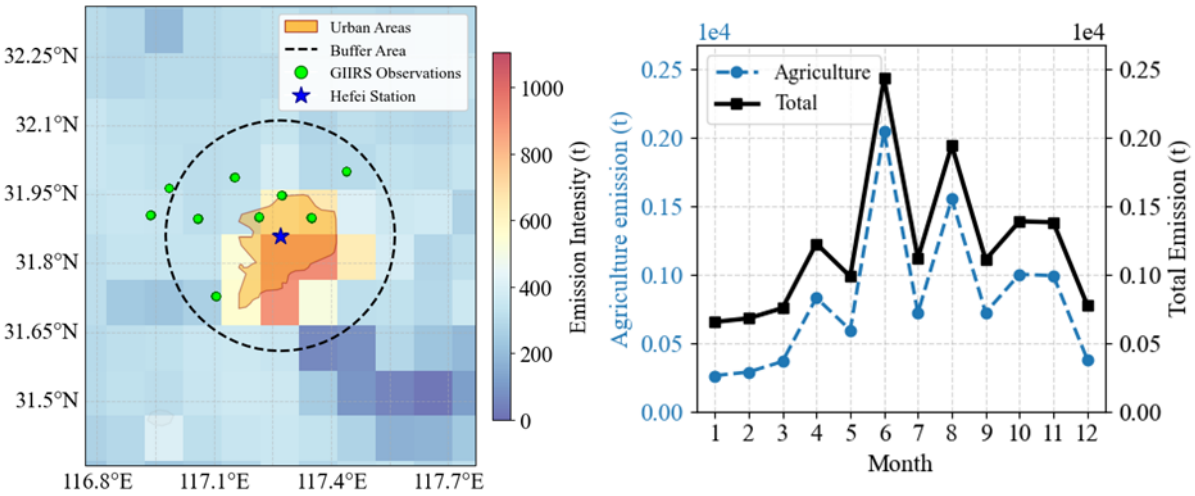

Figure S10. Spatial and temporal pattern of ammonia emissions in 2017 from the MIX emission inventory at the Hefei station. (a) Spatial distribution of anthropogenic NH_3 emissions and GIIRS observations. The green points represent locations where GIIRS observations were repeatedly acquired and the corresponding NH_3 retrievals satisfied the filtering criteria applied in this study. (b) Monthly timeseries of anthropogenic NH_3 emissions. The blue stars indicate the locations of Hefei station (31.91°N, 117.17°E), as described in Sect. 3.2.

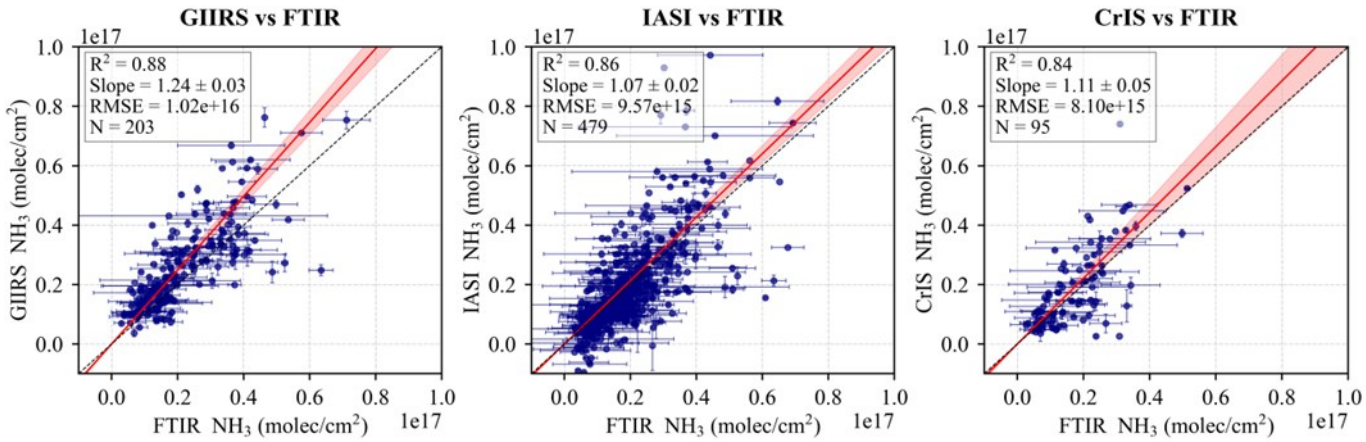

Figure S11. Same as Figure 8, but using the Orthogonal Distance Regression (ODR) method to fit hourly NH_3 columns from GIIRS, IASI, and CrIS to FTIR observations at the Hefei station.

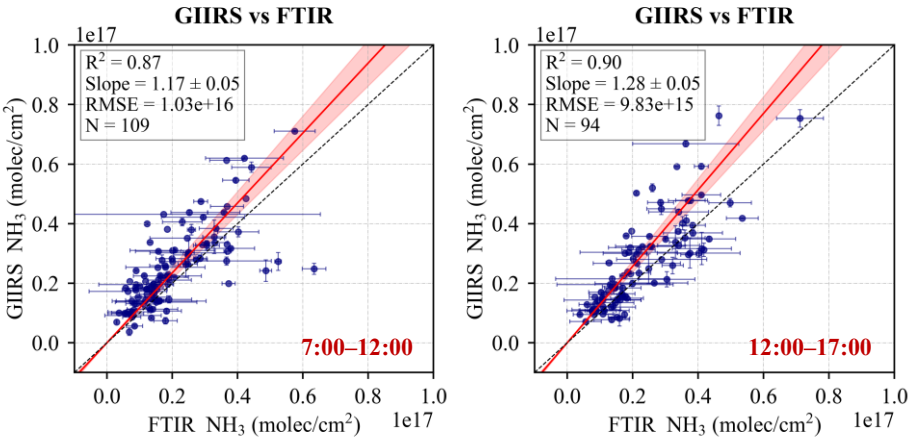

Figure S12. Cross-validation of GIIRS and FTIR from 8:00–12:00 and 12:00–16:00 using the Orthogonal Distance Regression (ODR) method.

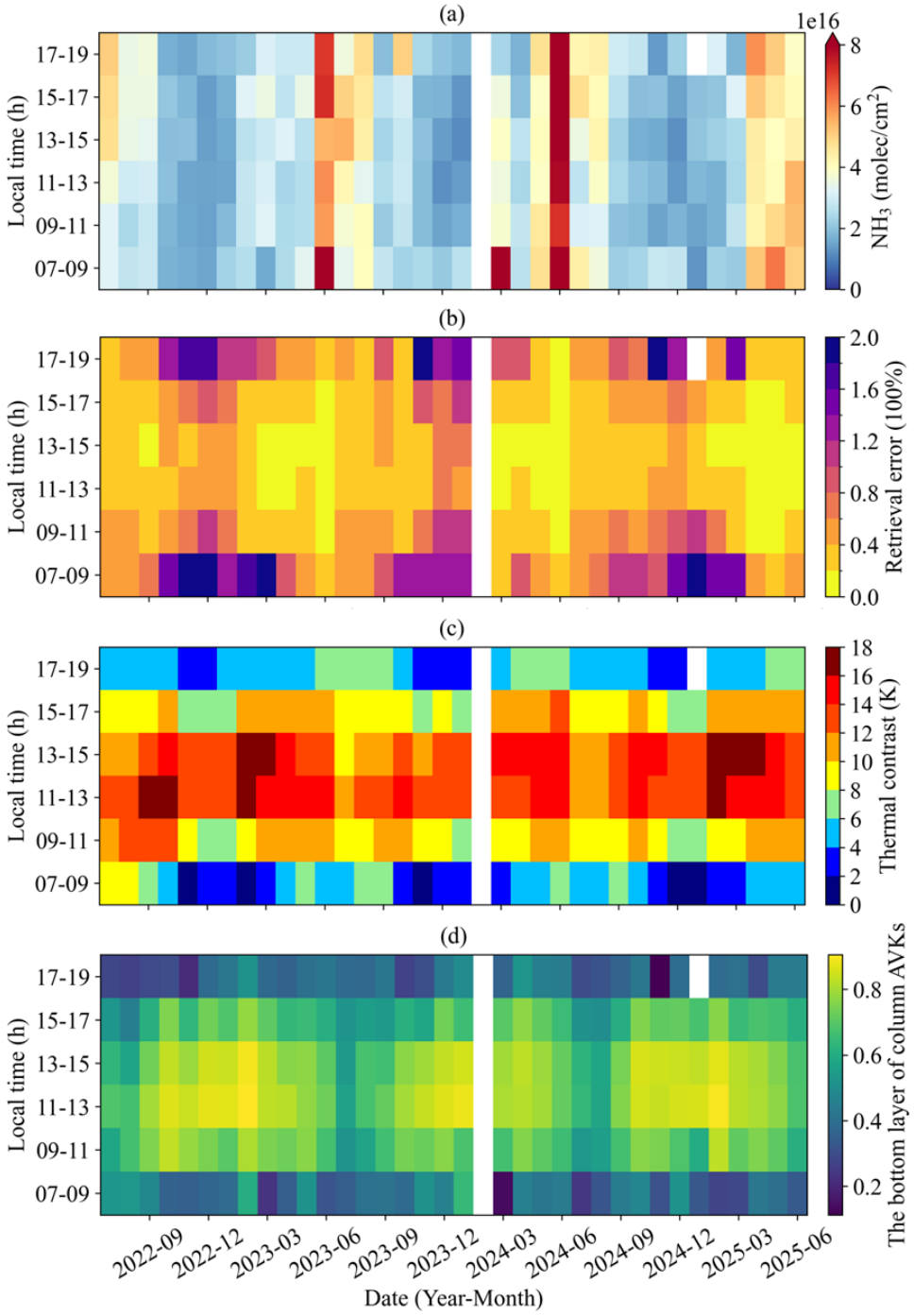

Figure S13. Temporal variations of (a) NH_3 columns, (b) the corresponding retrieval error, (c) TC, and (d) the bottom layer of column AVKs. These statistics are calculated from FY-4B/GIIRS NH_3 retrievals within a 0.25° latitude/longitude radius around the Hefei station.

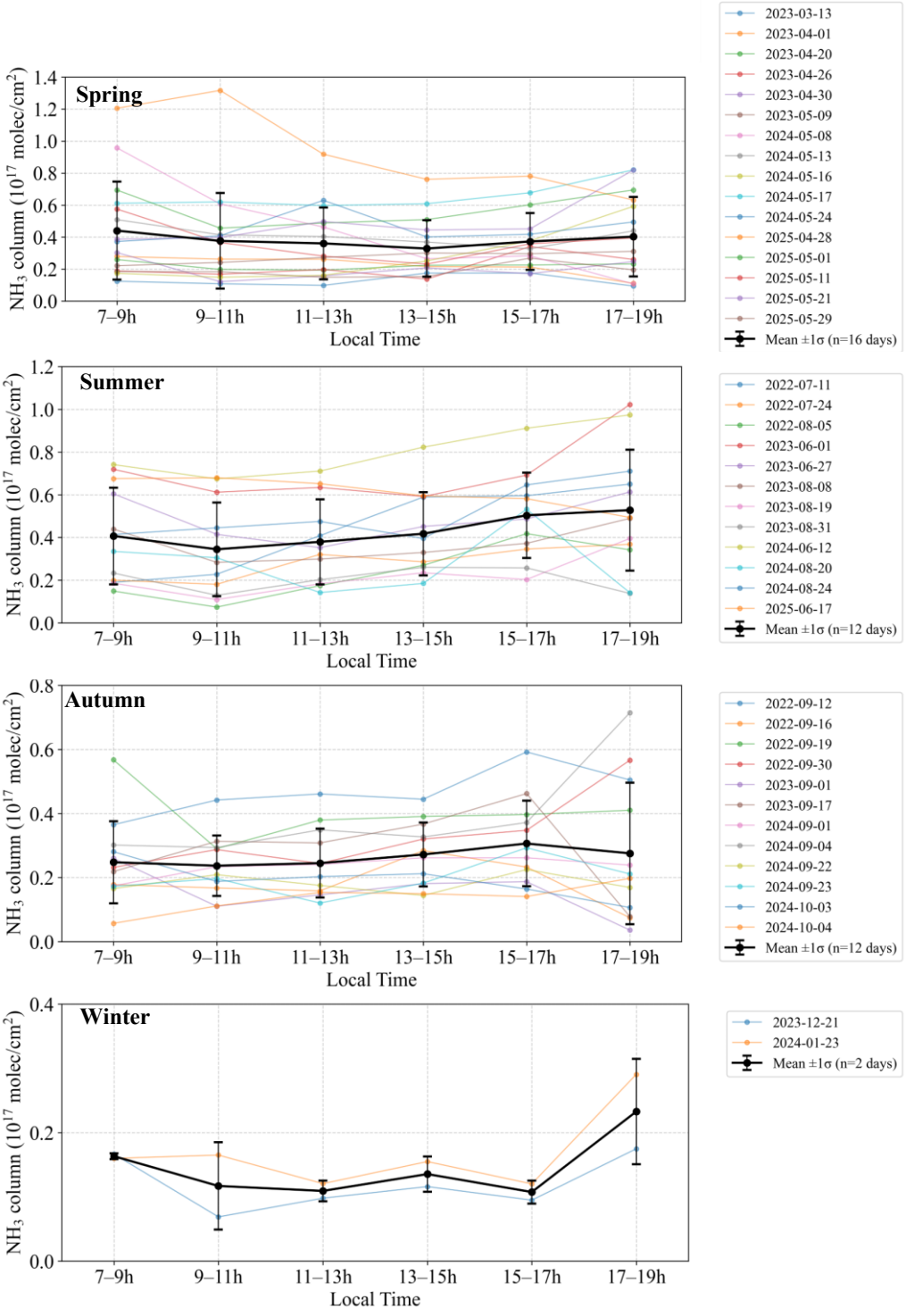

Figure S14. Daytime NH_3 variations observed by FY-4B/GIIRS from 37 high-quality observation days.

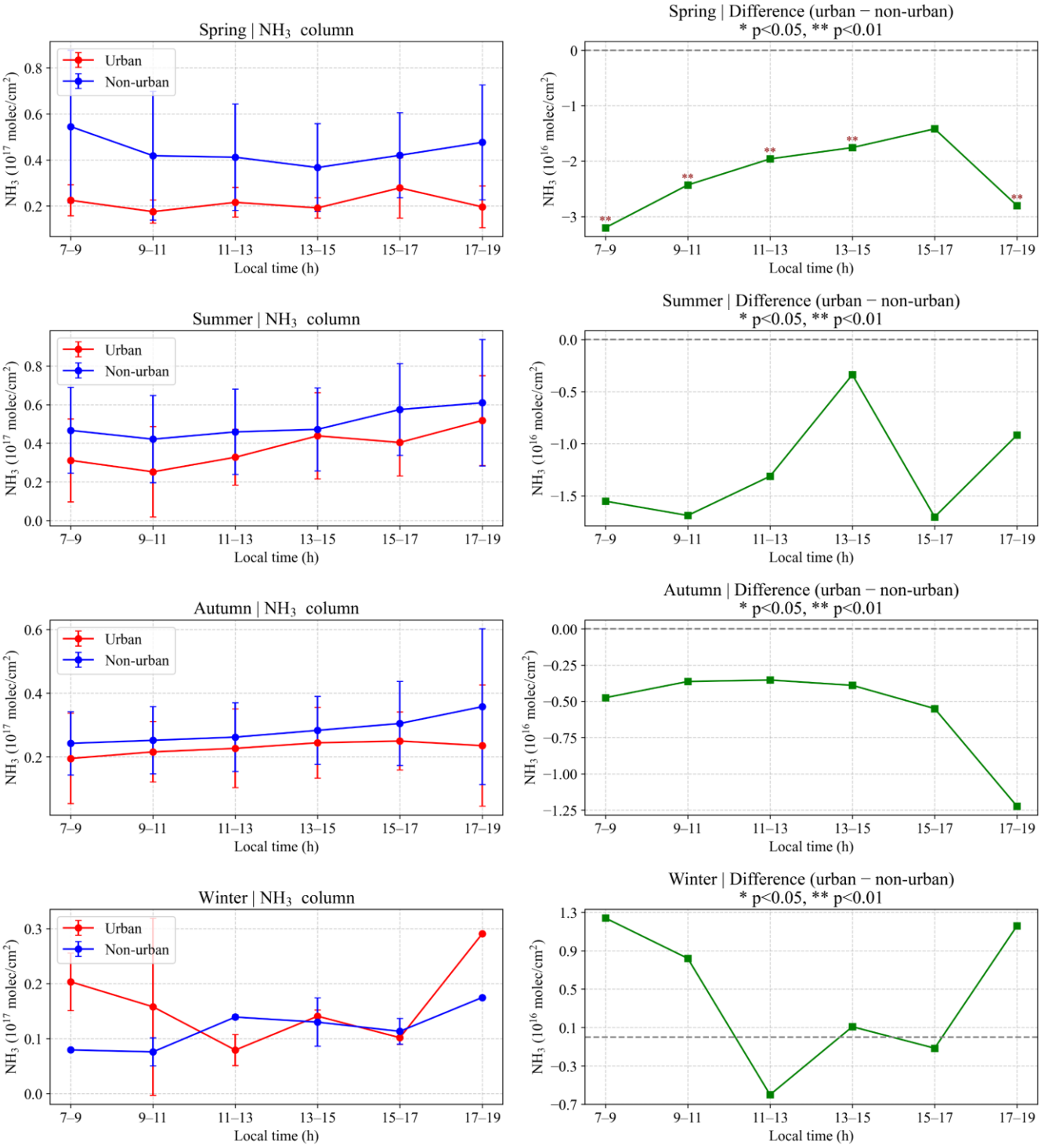

Figure S15. Daytime NH_3 variations observed by GIIRS at the Hefei station in different seasons for urban areas and non-urban areas.

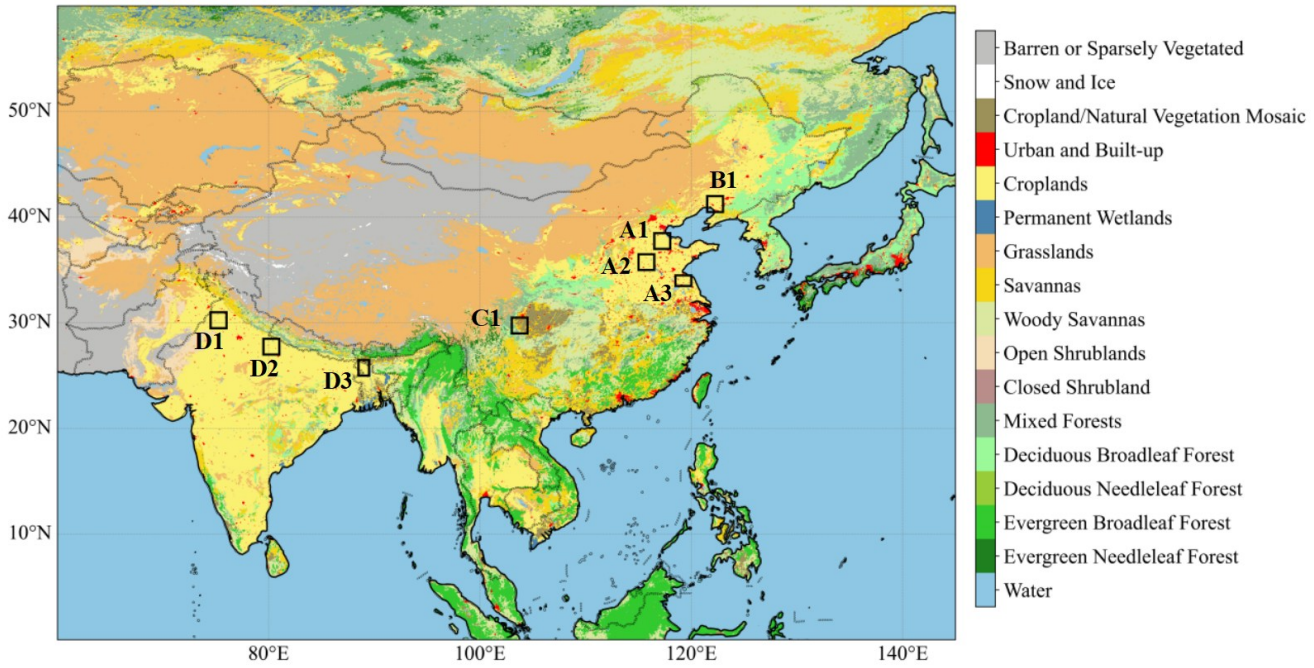

Figure S16. Spatial distribution of land cover over East Asia in 2025 based on the Moderate Resolution Imaging Spectroradiometer (MODIS) MCD12C1 dataset (https://ladsweb.modaps.eosdis.nasa.gov/, accessed March 19 2026). Black boxes indicate the eight agricultural source areas analyzed in Sect. 3.3.

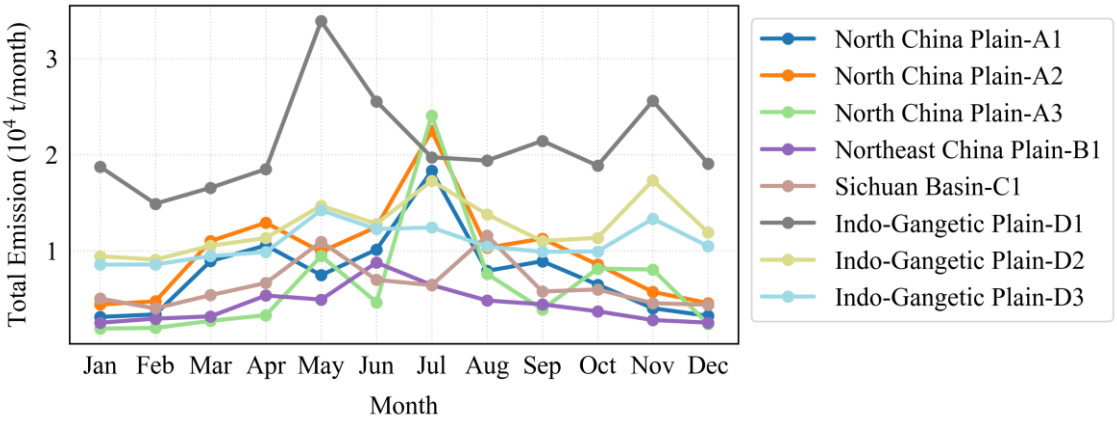

Figure S17. Monthly variations of NH_3 total emissions from the MIX inventory (2017) for eight agricultural source areas.

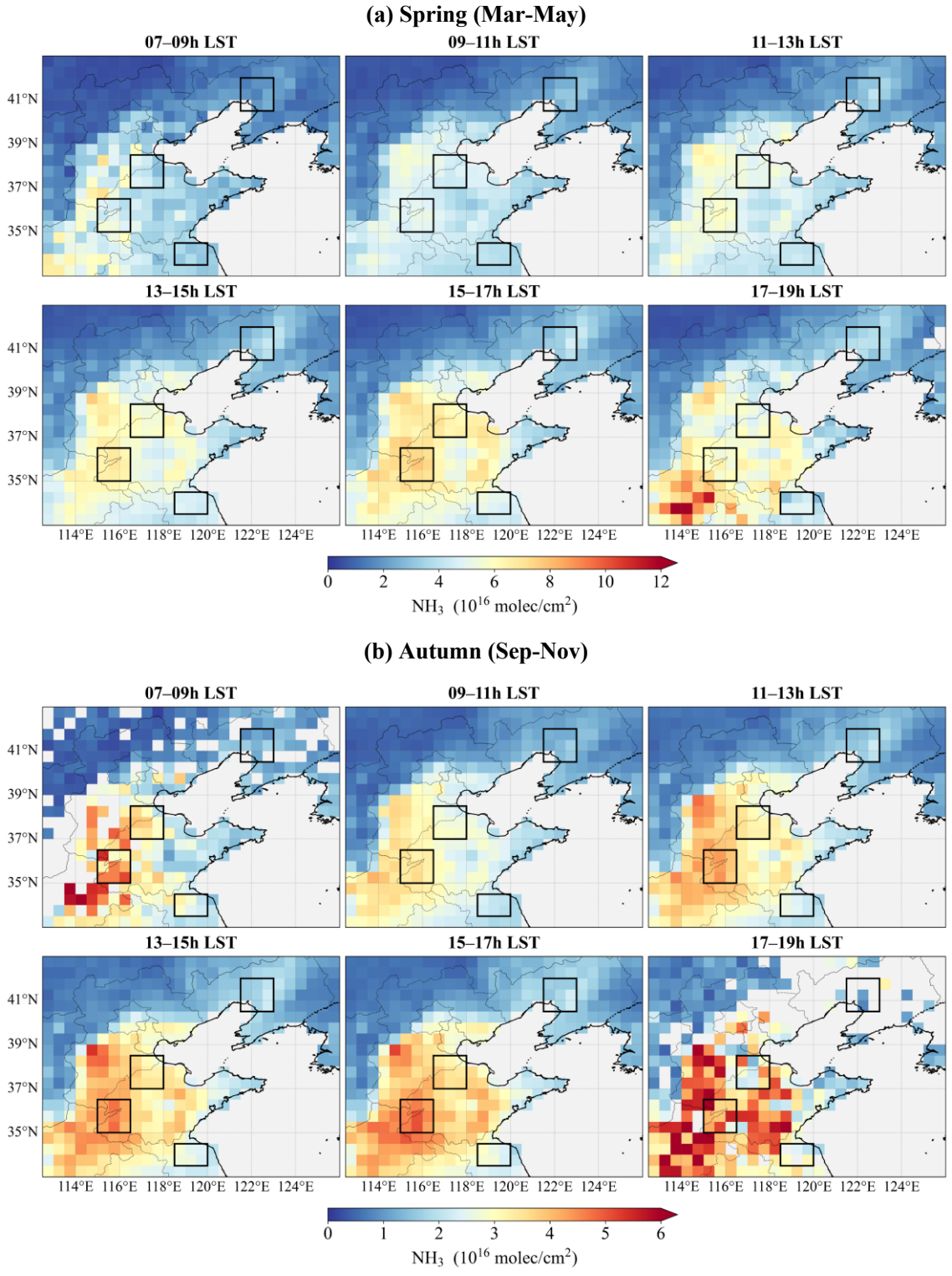
(a) Spring (Mar-May)
07–09h LST
09–11h LST
11–13h LST
13–15h LST
15–17h LST
17–19h LST
41°N
39°N
37°N
35°N
114°E 116°E 118°E 120°E 122°E 124°E
0 2 4 6 8 10 12
NH3 (10^16 molec/cm^2)
(b) Autumn (Sep-Nov)
07–09h LST
09–11h LST
11–13h LST
13–15h LST
15–17h LST
17–19h LST
41°N
39°N
37°N
35°N
114°E 116°E 118°E 120°E 122°E 124°E
0 1 2 3 4 5 6
NH3 (10^16 molec/cm^2)

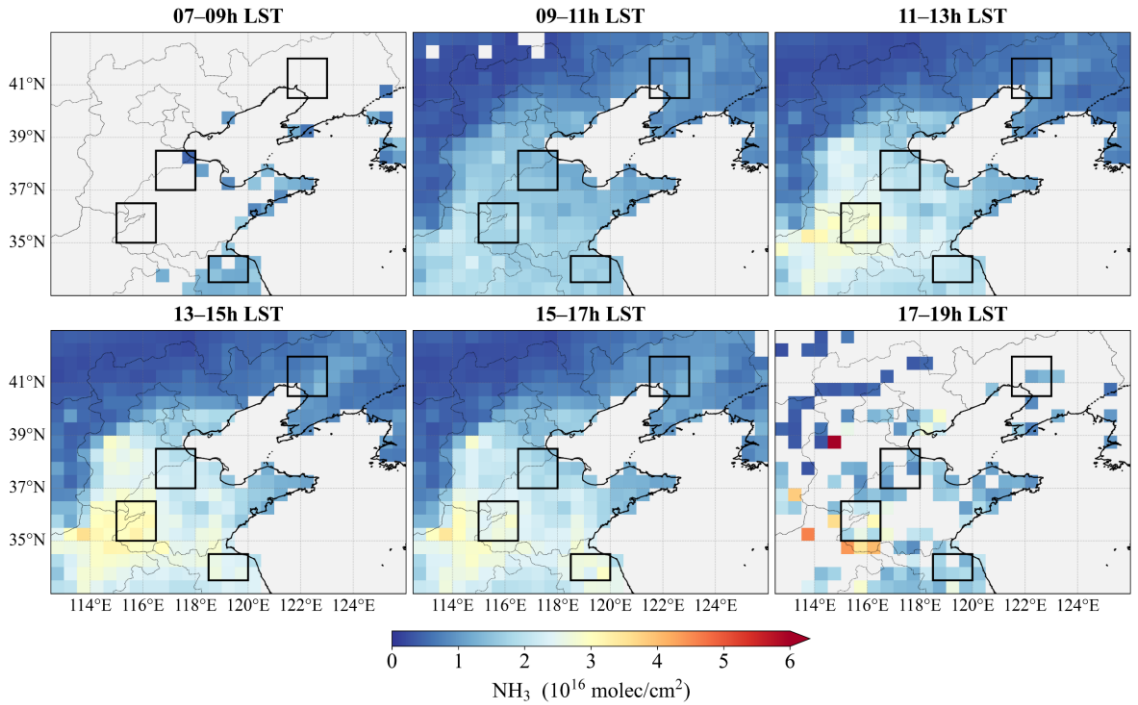

Figure S18. Daytime NH_3 variations observed by GIIRS from July 2022 to June 2025 in the North-Northeast China Plains for different seasons.

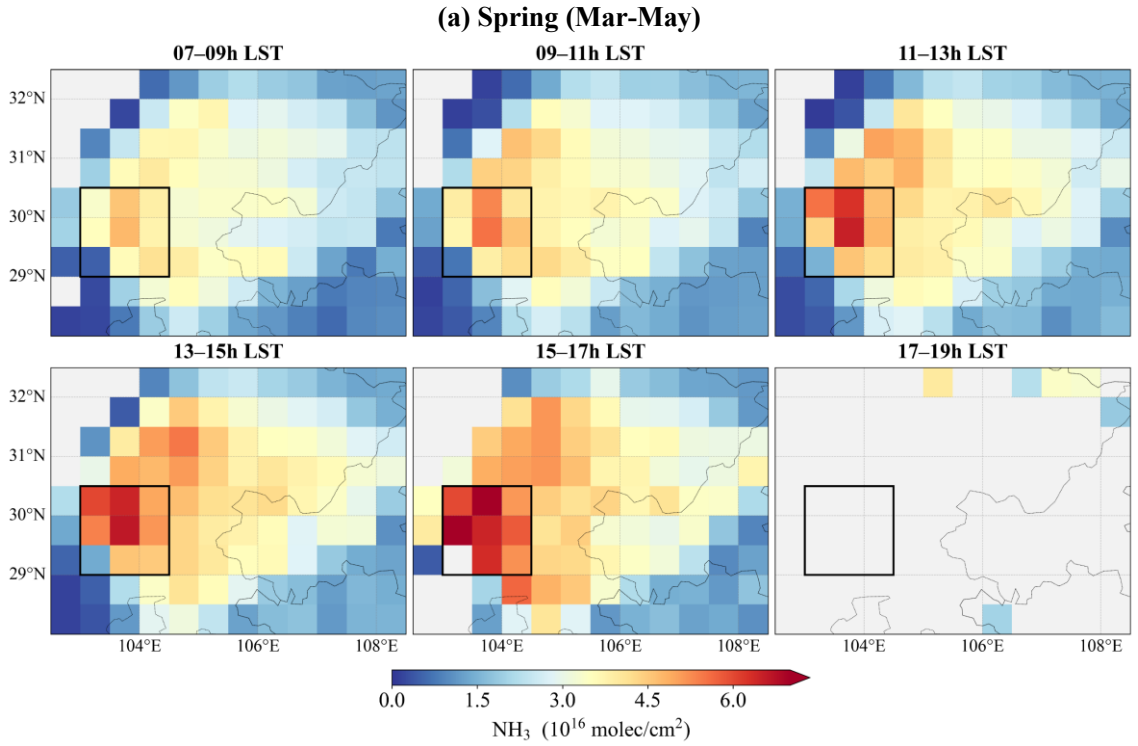
(a) Spring (Mar-May)
07–09h LST
09–11h LST
11–13h LST
13–15h LST
15–17h LST
17–19h LST
32°N
31°N
30°N
29°N
104°E
106°E
108°E
0.0
1.5
3.0
4.5
6.0
NH3 (10^16 molec/cm^2)

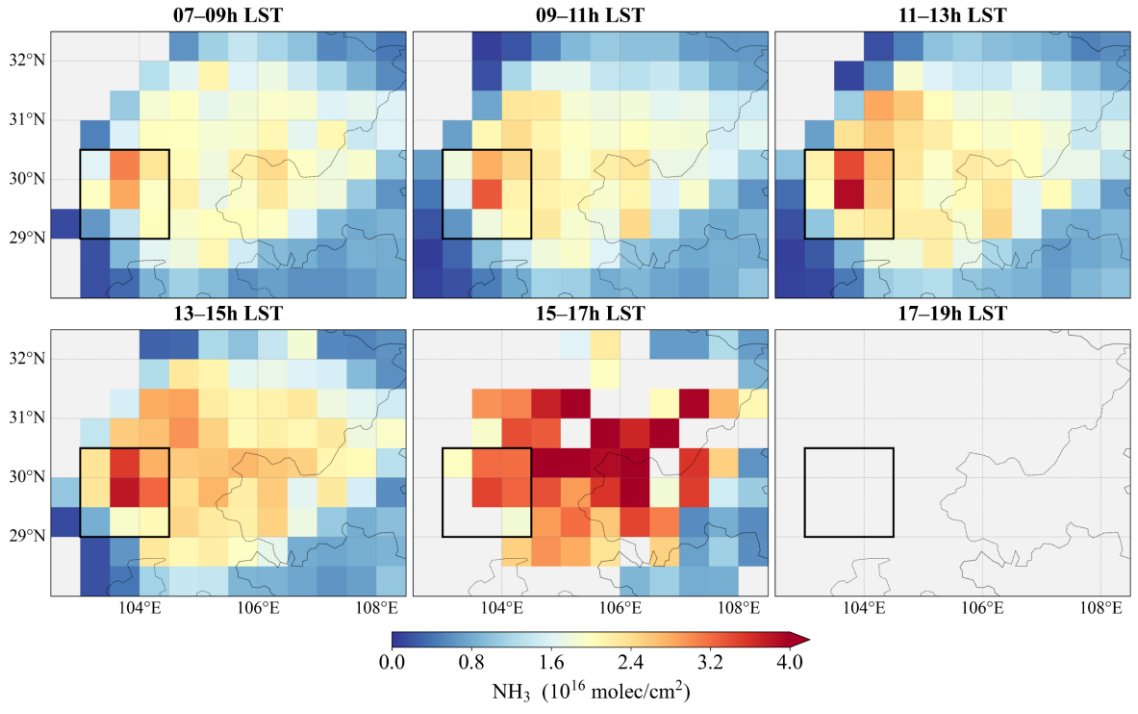
(b) Autumn (Sep-Nov)
07–09h LST
09–11h LST
11–13h LST
13–15h LST
15–17h LST
17–19h LST
32°N
31°N
30°N
29°N
104°E
106°E
108°E
0.0
0.8
1.6
2.4
3.2
4.0
NH3 (10^16 molec/cm^2)

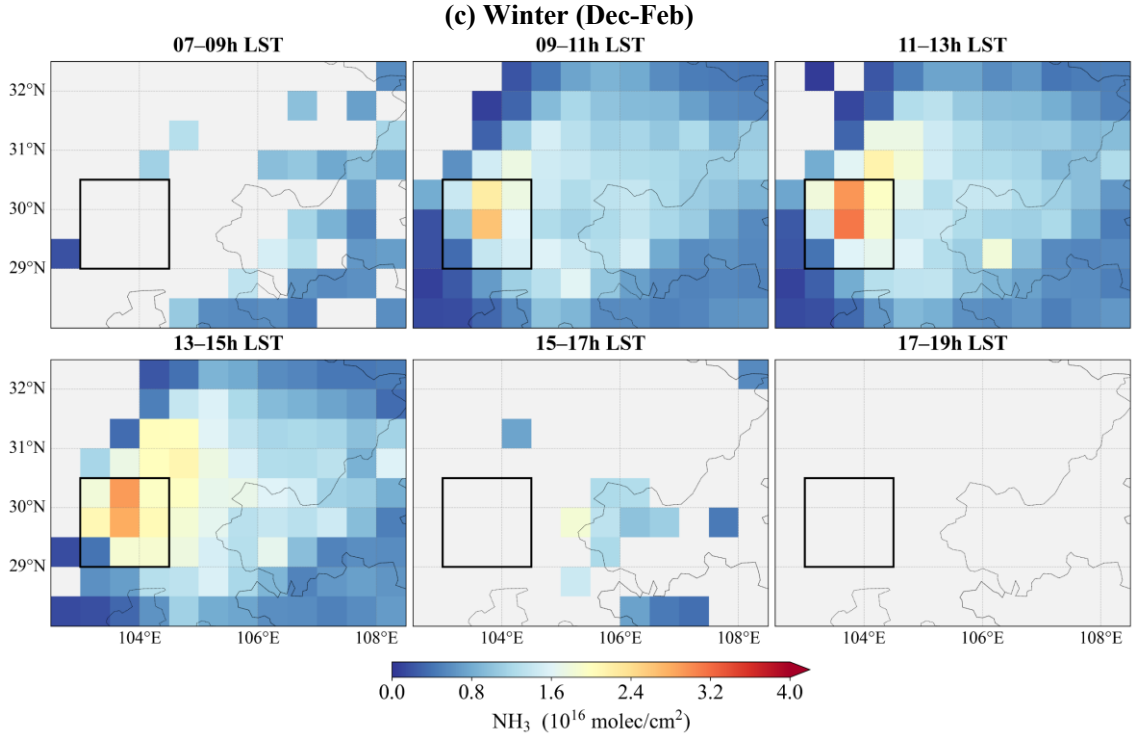

Figure S19. Daytime NH_3 variations observed by GIIRS from July 2022 to June 2025 in the Sichuan Basin for different seasons.

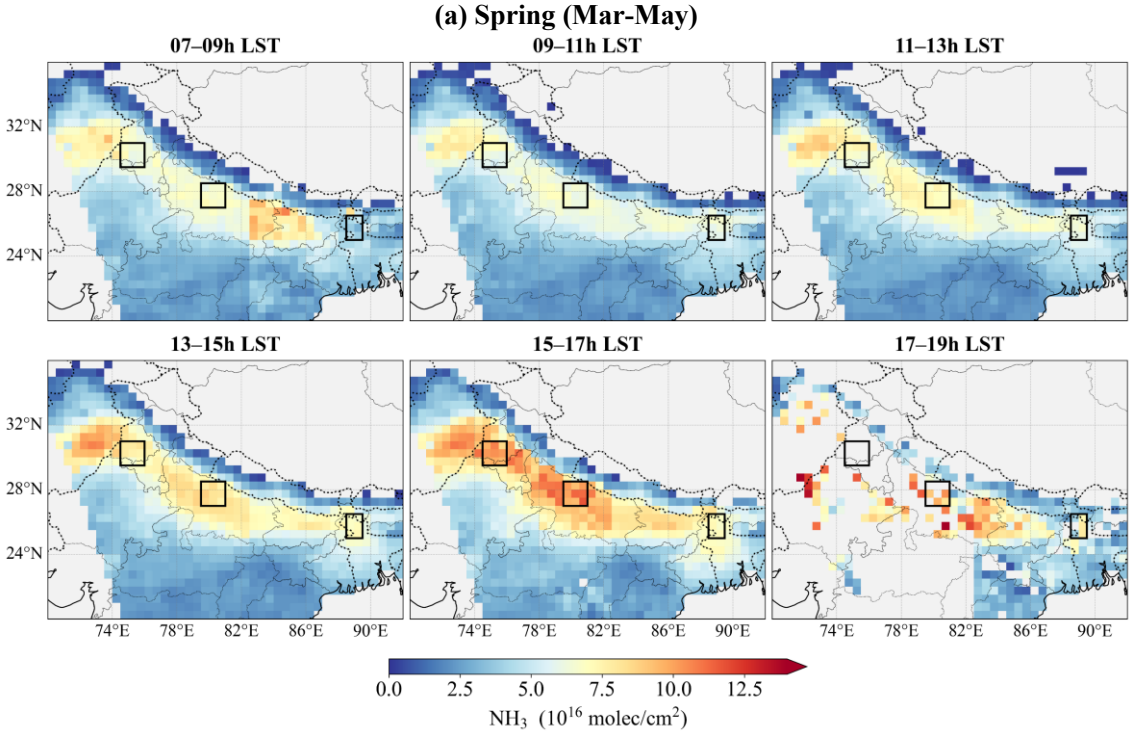
(a) Spring (Mar-May)
07–09h LST
09–11h LST
11–13h LST
13–15h LST
15–17h LST
17–19h LST
32°N
28°N
24°N
74°E
78°E
82°E
86°E
90°E
0.0
2.5
5.0
7.5
10.0
12.5
NH3 (10^16 molec/cm2)

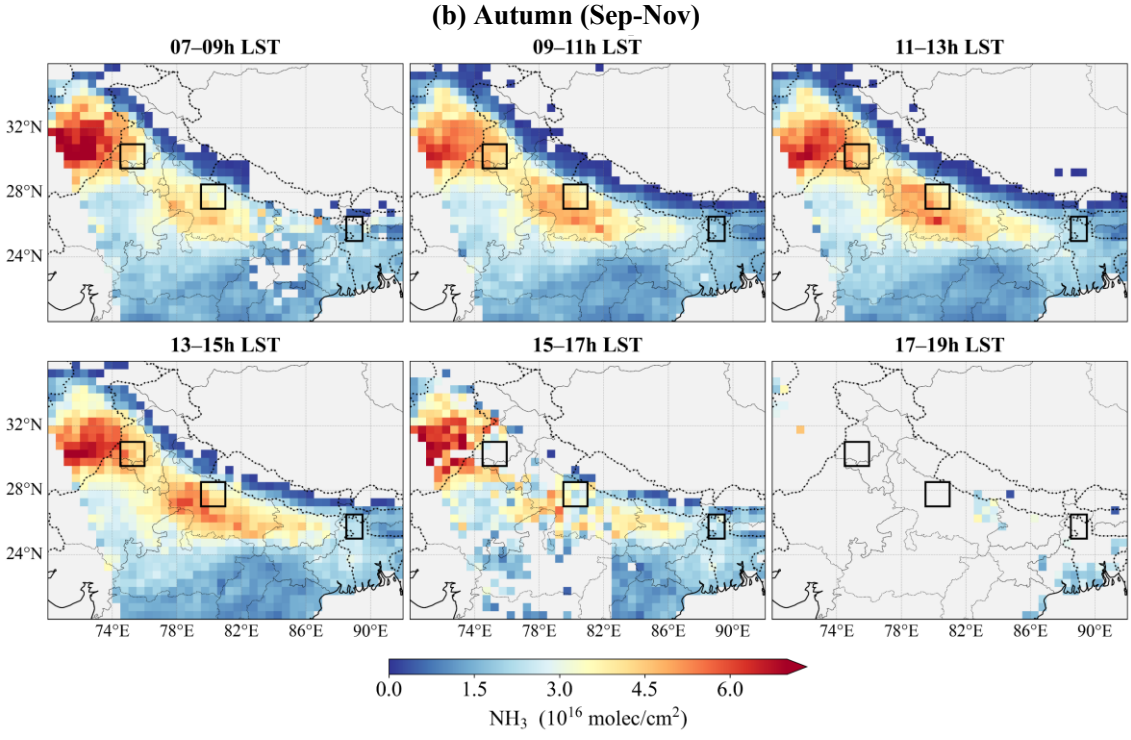
(b) Autumn (Sep-Nov)
07–09h LST
09–11h LST
11–13h LST
13–15h LST
15–17h LST
17–19h LST
32°N
28°N
24°N
74°E
78°E
82°E
86°E
90°E
0.0
1.5
3.0
4.5
6.0
NH3 (10^16 molec/cm2)

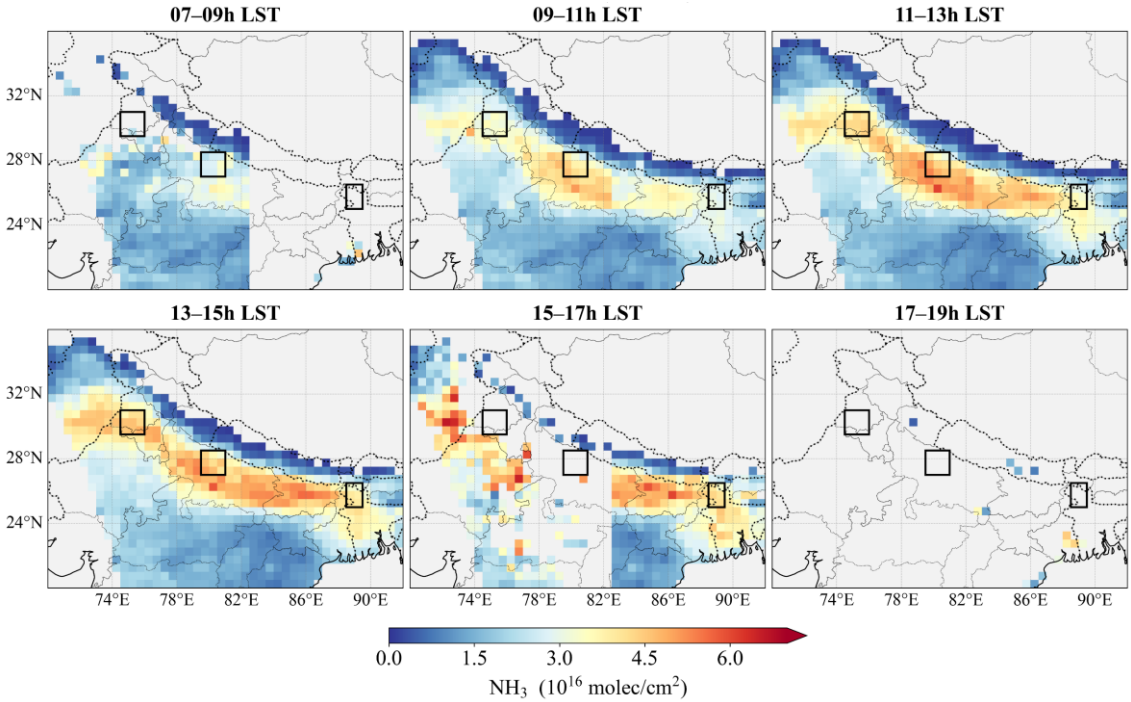

Figure S20. Daytime NH_3 variations observed by GIIRS from July 2022 to June 2025 in the Indo-Gangetic Gangetic Plain for different seasons.

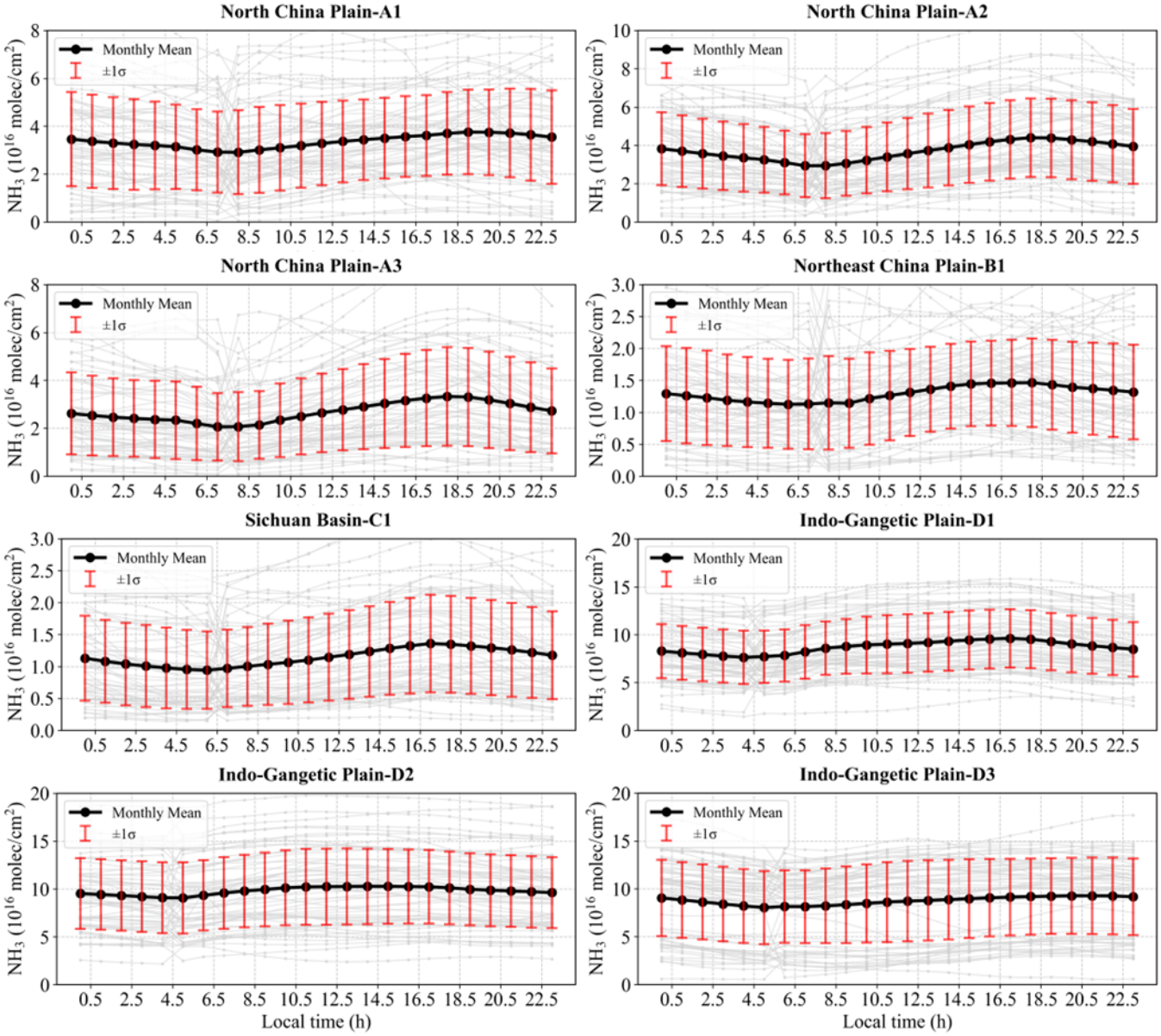

Figure S21. Diurnal NH_3 variations in May and June 2025 from GEOS-CF model in the major agricultural areas.

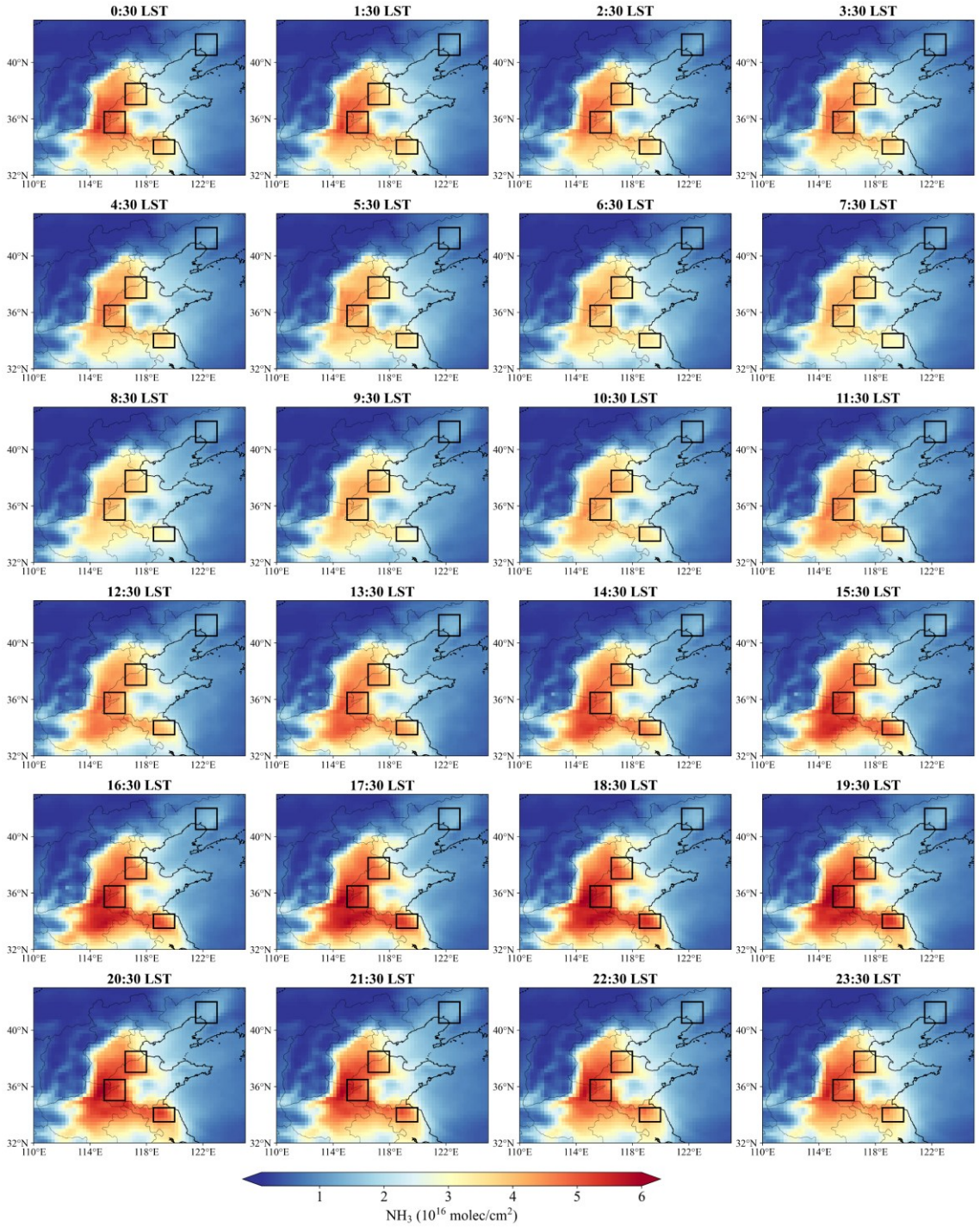

Figure S22. Spatial pattern of NH_3 columns from GEOS-CF model in May and June 2025 over the North China Plain and the Northeast China Plain.

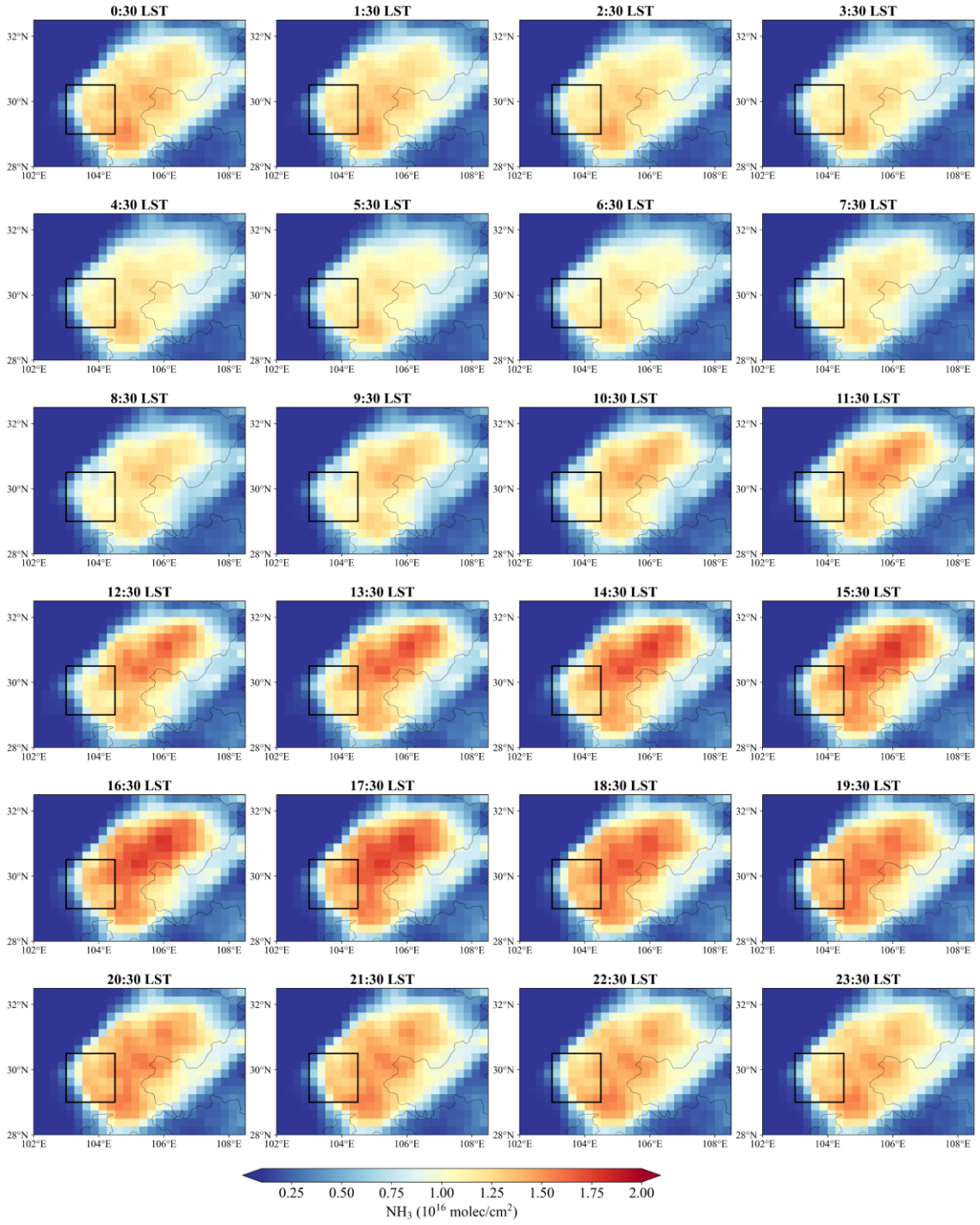

Figure S23. Spatial pattern of NH_3 columns from GEOS-CF model in May and June 2025 over the Sichuan Basin.

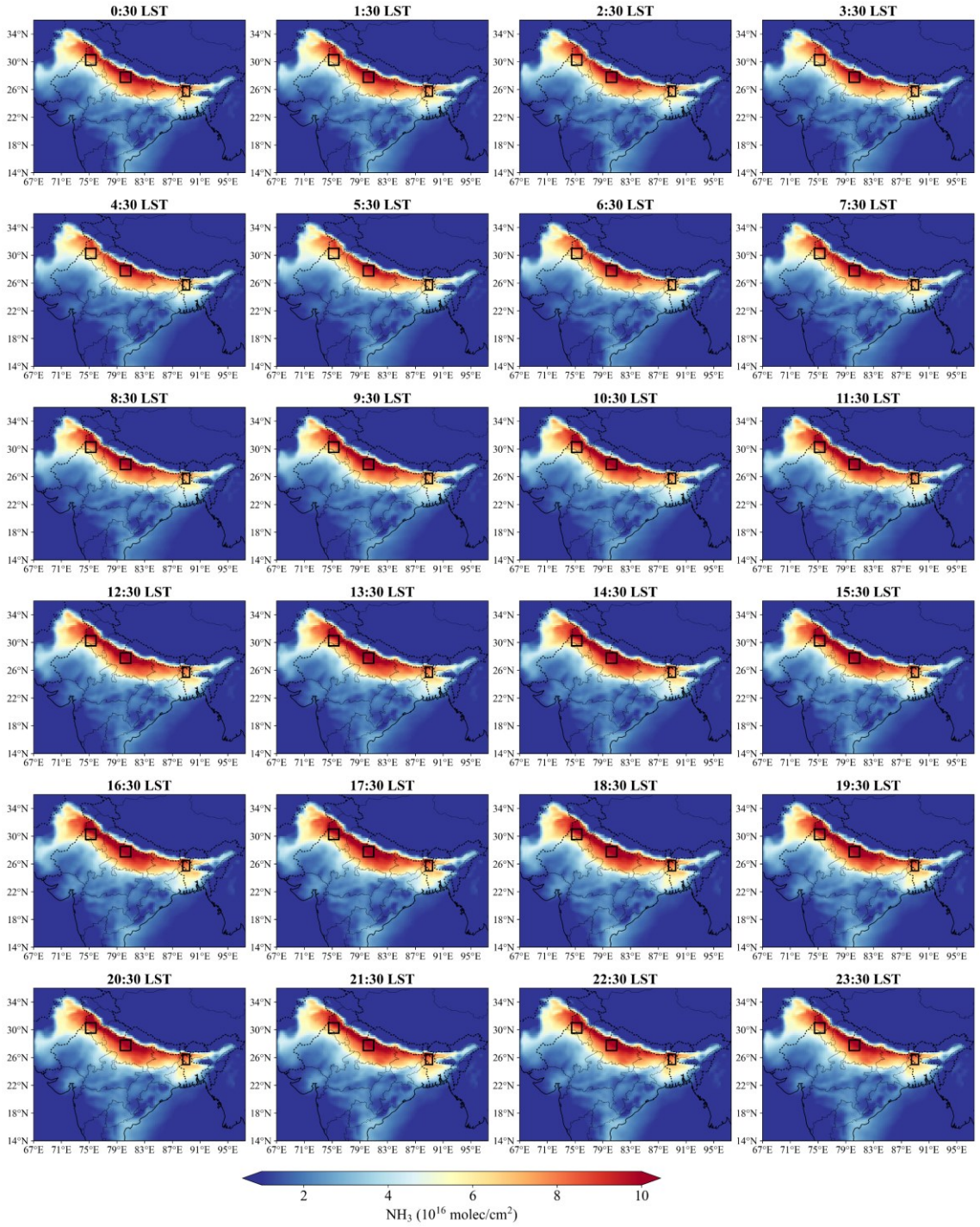

Figure S24. Spatial pattern of NH_3 columns from GEOS-CF model in May and June 2025 over the Indo-Gangetic Plain.

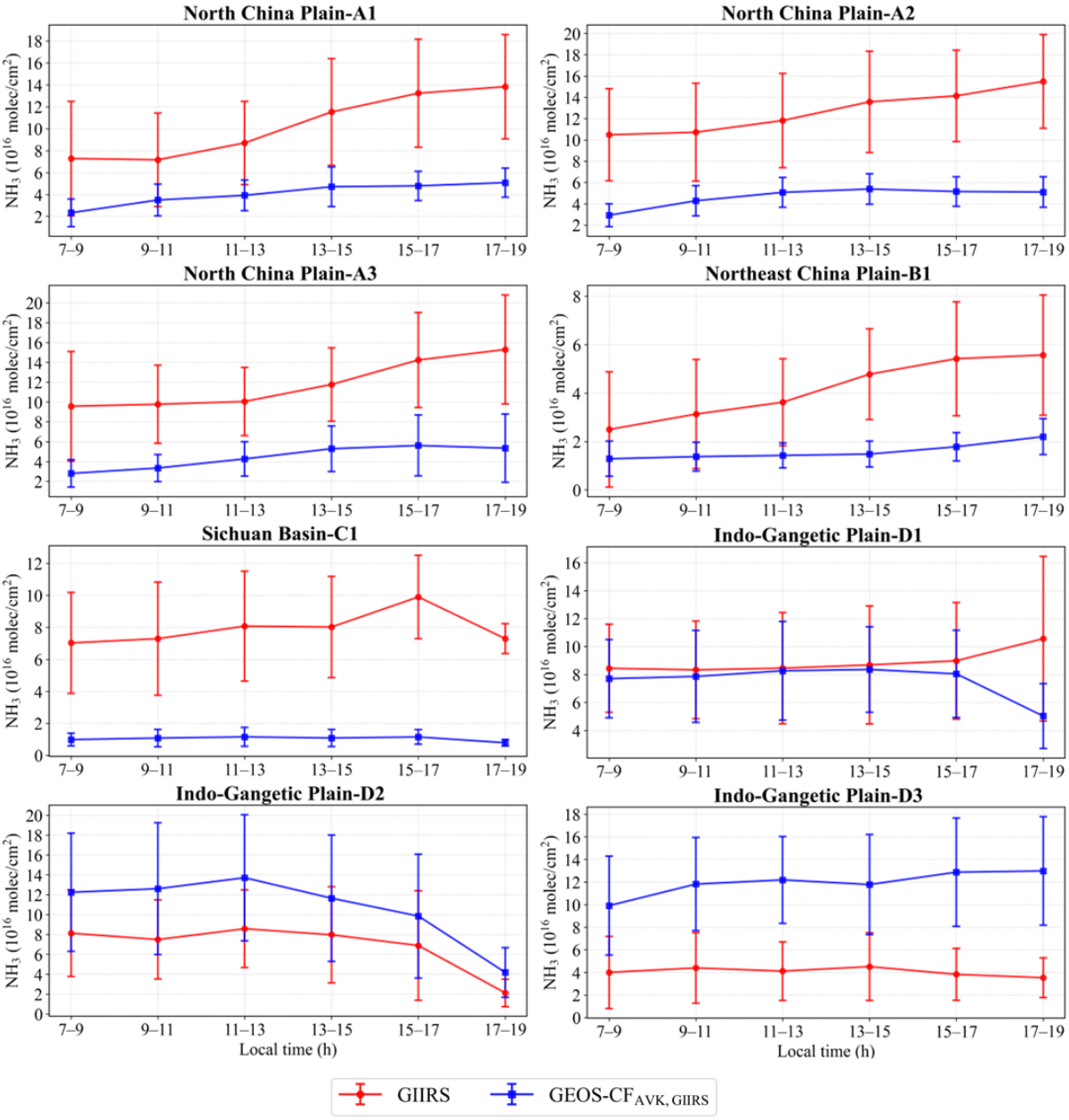

Figure S25. Diurnal NH_3 variations in May and June 2025 from GEOS-CF AVK-smoothed model data in the major agricultural areas.

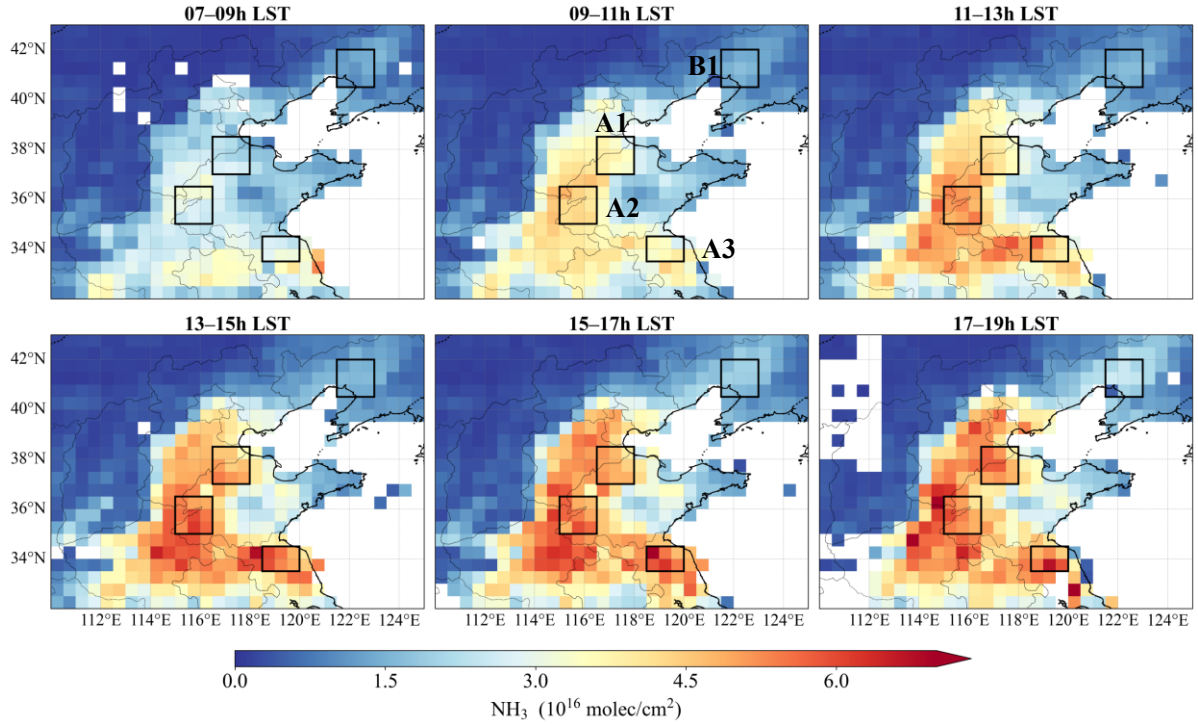

Figure S26. Spatial pattern of GEOS-CF AVK-smoothed model data in May and June 2025 over the North China Plain and the Northeast China Plain.

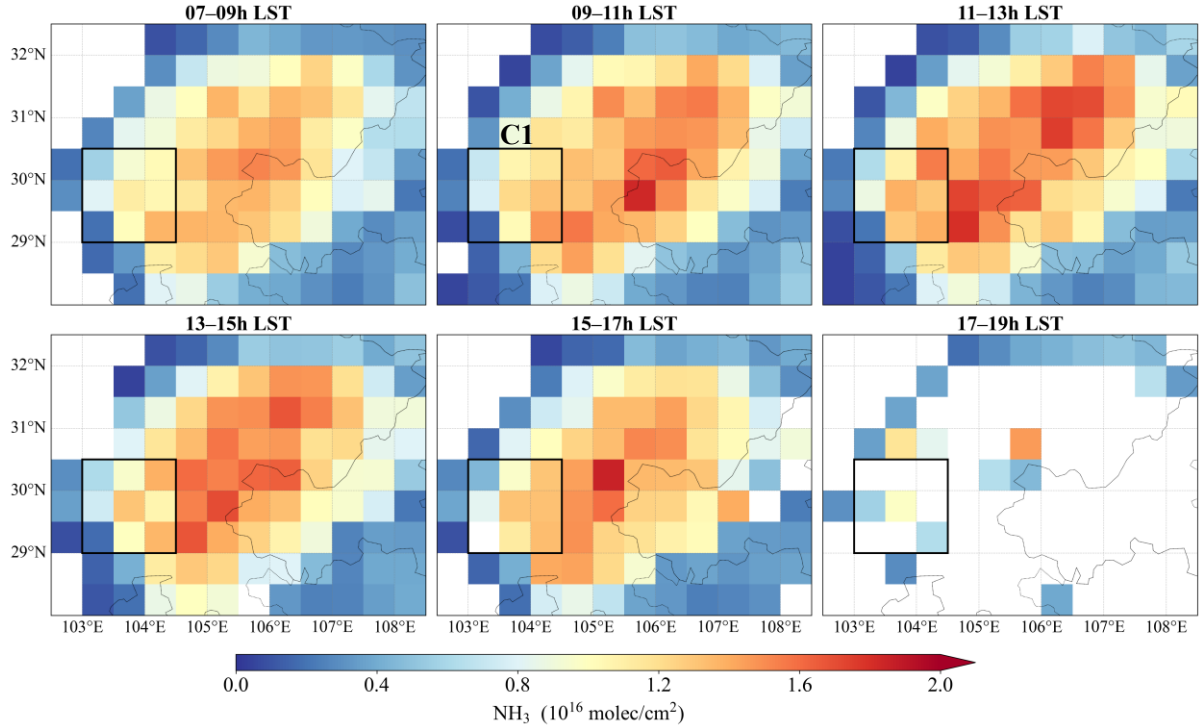

Figure S27. Spatial pattern of GEOS-CF AVK-smoothed model data in May and June 2025 over the Sichuan Basin.

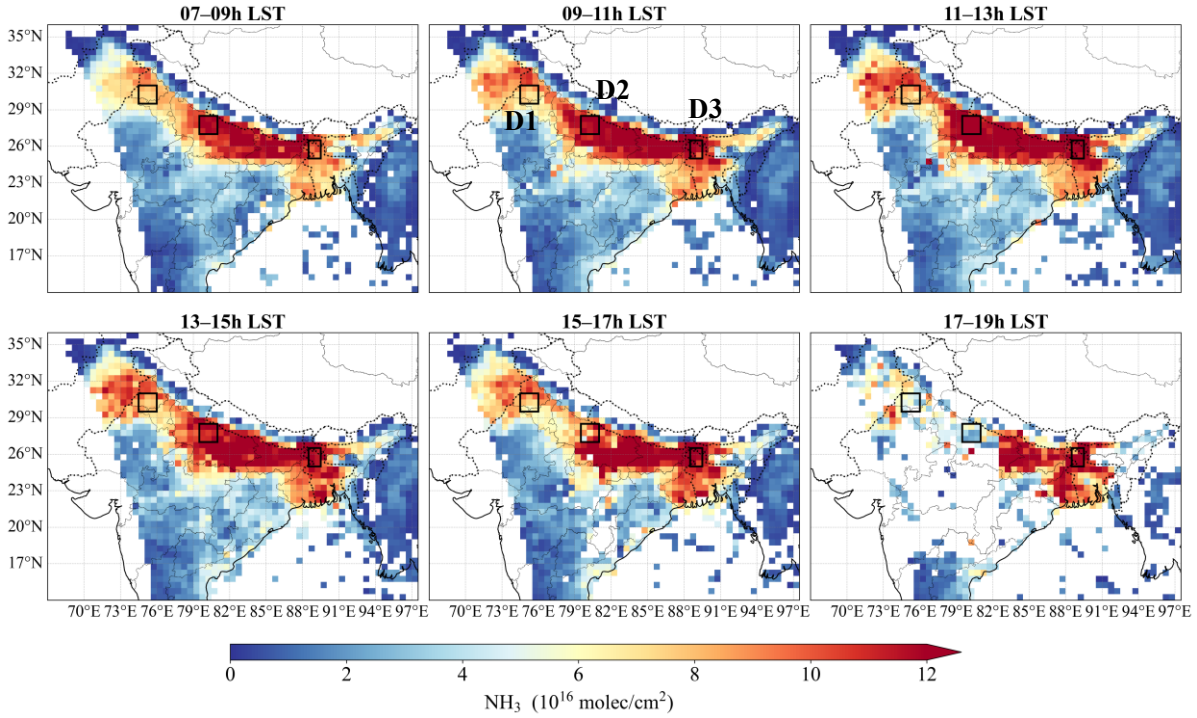

Figure S28. Spatial pattern of GEOS-CF AVK-smoothed model data in May and June 2025 over the Indo-Gangetic Plain.